PHYSICAL REVIEW B **96**, 165104 (2017)

Hund's coupling driven photocarrier relaxation in the two-band Mott insulator

Hugo U. R. Strand,[1,2,*] Denis Golež,[2] Martin Eckstein,[3] and Philipp Werner[2,†]
[1]*Department of Quantum Matter Physics, University of Geneva, 24 Quai Ernest-Ansermet, 1211 Geneva 4, Switzerland*
[2]*Department of Physics, University of Fribourg, 1700 Fribourg, Switzerland*
[3]*Department of Physics, University of Erlangen-Nürnberg, 91058 Erlangen, Germany*

(Received 21 April 2017; revised manuscript received 4 August 2017; published 3 October 2017)

We study the relaxation dynamics of photocarriers in the paramagnetic Mott insulating phase of the half-filled two-band Hubbard model. Using nonequilibrium dynamical mean-field theory, we excite charge carriers across the Mott gap by a short hopping modulation, and simulate the evolution of the photodoped population within the Hubbard bands. We observe an ultrafast charge-carrier relaxation driven by the emission of local spin excitations with an inverse relaxation time proportional to the Hund's coupling. The photodoping generates additional side-bands in the spectral function, and for strong Hund's coupling, the photodoped population also splits into several resonances. The dynamics of the local many-body states reveals two effects, *thermal blocking* and *kinetic freezing*, which manifest themselves when the Hund's coupling becomes of the order of the temperature or the bandwidth, respectively. These effects, which are absent in the single-band Hubbard model, should be relevant for the interpretation of experiments on correlated materials with multiple active orbitals. In particular, the features revealed in the nonequilibrium energy distribution of the photocarriers are experimentally accessible, and provide information on the role of the Hund's coupling in these materials.

DOI: 10.1103/PhysRevB.96.165104

I. INTRODUCTION

The photoexcitation of charge carriers across a Mott or charge-transfer gap triggers a nonequilibrium phase transition from a correlation-induced insulating to a nonthermal conducting state. A wide range of experiments have characterized these photodoped metallic states and explored the relaxation pathways and lifetimes of the photocarriers, as well as their effect on ordered states. Iwai and collaborators [1] measured the reflectivity spectrum of a nickel-chain compound, and found that it exhibits a Drude-like low-energy feature immediately after photoexcitation and that this metallic behavior lasts for several picoseconds. Similar results have also been obtained for the cuprates La_2CuO_4 and Nd_2CuO_4 [2], where it was also shown that charge-spin and charge-phonon couplings play an important role in the short-time relaxation process. Using time-resolved photoemission spectroscopy, the ultrafast relaxation of photodoped doublons has been investigated in the polaronic Mott insulator $1T$-TaS_2 [3–5], and femtosecond resonant x-ray diffraction has been employed to study the effect of photodoping on the magnetic structure in CuO [6] and $TbMnO_3$ [7]. The latter material exhibits a complex interplay between charge, spin, and orbital degrees of freedom.

Unveiling the nature of the bosonic excitations coupled to the electronic degrees of freedom is one of the fundamental goals of pump-probe spectroscopy. The two-temperature model introduced by Allen [8] provides a means to extract the microscopical parameters describing electron-phonon coupling from the relaxation dynamics after photoexcitation [9,10]. A careful analysis of time-dependent optical spectroscopy [11] and angle-resolved photoemission spectroscopy (ARPES) measurements [12] enabled the determination of the relative weight of the electron-boson coupling for a broad range of frequencies [13,14]. The population dynamics measured in ARPES furthermore allows to disentangle the electron-electron interactions from electron-boson interactions [12]. This information is crucial for determining the microscopic origin of symmetry broken states, such as superconductivity [14], density-wave orders [15], excitonic insulators, etc., especially when several orders are intertwined [16].

Significant theoretical effort has also been aimed at understanding the basic aspects of the photodoping process and the subsequent relaxation [17–19]. These studies—which so far have focused on single-band models—have addressed the exponential dependence of the photocarrier's lifetime on the Mott gap [19–21], the role of impact ionization processes in small-gap insulators [22], and the nature of the photodoped metallic state [23]. Deep in the Mott phase the number of holon-doublon pairs is an almost conserved quantity on the time scale of the electronic hopping, and the initial relaxation of the photocarriers can only occur within the Hubbard bands. The corresponding relaxation time strongly depends on the coupling of the photodoped carriers to bosonic degrees of freedom, such as spins [24,25] or phonons [26–30]. In particular, the scattering with antiferromagnetically ordered spins provides a very efficient cooling mechanism [14,24,31,32]. Very strong electron-boson couplings, which appear, for example, in systems with dynamically screened Coulomb interactions [33], can on the other hand open new channels for doublon-hole recombination and lead to a nontrivial energy exchange between electronic and bosonic degrees of freedom [26,33,34].

In multiorbital Hubbard systems, one should expect similar processes to play a prominent role even in the absence of phonon couplings, antiferromagnetic correlations, and nonlocal interactions. In Mott insulators with small or vanishing crystal-field splitting, the Hund's coupling controls the energies of the most relevant local states, and favors high-spin states. The goal of this study is to clarify how photodoped carriers moving in this high-spin background produce local

---

[*] hugo.strand@gmail.com

[†] philipp.werner@unifr.ch

2469-9950/2017/96(16)/165104(16)

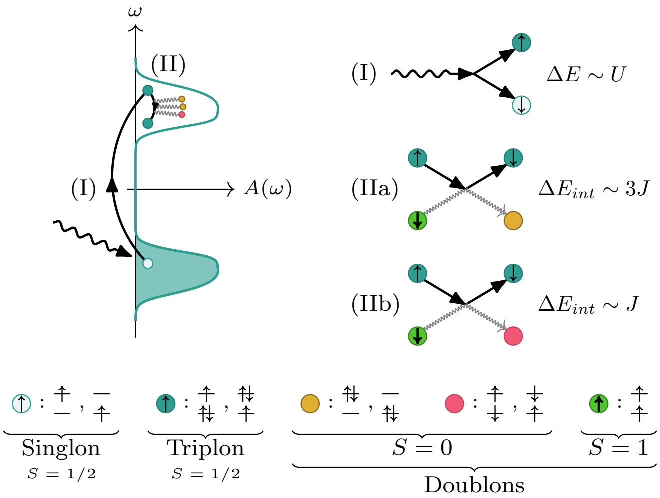

FIG. 1. Schematic illustration of the photodoping process in a two-band Mott insulator, creating photoexcited singlon-triplon pairs (I), and the subsequent relaxation by doublon-triplon (and doublon-singlon) scattering (II), which generates high-energy (IIa), and low-energy (IIb) $S = 0$ doublon excitations on the $S = 1$ high-spin doublon background. A legend for the local two-orbital states is shown at the bottom.

spin excitations and thereby transfer their excess kinetic energy to interaction energy.

We will explore this physics in the simple context of a half-filled two-orbital Mott insulator with degenerate bands and density-density interactions. For positive Hund's coupling J, the dominant states are the half-filled high spin states ($[\uparrow,\uparrow]$) indicated by the green dots in Fig. 1, while the two low-spin states ($[\uparrow,\downarrow]$ and $[\uparrow\downarrow,0]$) have an energy that is higher by J (red dots) and $3J$ (yellow dots), respectively. Driving the system with a frequency above the interorbital interaction U produces photocarriers in terms of singlon-triplon pairs, as illustrated by process (I) of Fig. 1. The singlons and triplons, with an initially high kinetic energy, then scatter with the high-spin doublon states transferring energy quanta of J (process IIa) or $3J$ (process IIb) to local spin excitations. As a result of this, the energy distributions of the triplons changes, and the corresponding population shifts within the upper Hubbard band towards the lower band edge. (An analogous dynamics takes place in the lower Hubbard band, where the singlon distribution shifts to the upper band edge.) We also observe a splitting of the photocarrier distribution in the upper Hubbard band, which can be linked to the Hund's coupling induced splitting of the local states within the doublon sector. By systematically studying the relaxation at a constant 1% photodoping as a function of temperature and Hund's coupling, we furthermore demonstrate two mechanisms, *thermal blocking* and *kinetic freezing* that partially inhibit the relaxation dynamics within the doublon sector.

This paper is organized as follows. Section II presents the effective two-band Hubbard model, and Sec. III presents the real-time dynamical mean-field method that we use to study the nonequilibrium dynamics. In Sec. IV, we present the equilibrium spectral function (Sec. IV A) and then discuss the photo doping dynamics (Sec. IV B). The different aspects of the relaxation dynamics are explored in the following sections: Sec. IV B 1 presents the simulated time-resolved photo emission spectra, while Sec. IV B 2 analyzes the short-time dynamics. The doublon excitation dynamics is discussed in Sec. IV B 3, and its temperature and Hund's coupling dependence in Secs. IV B 4 and IV B 5, respectively. Section V contains a discussion and conclusions.

II. MODEL

The two-band Hubbard model is the canonical model for interacting multiband electron systems, relevant, e.g., for the e_g irreducible representation of d-orbitals in crystal fields with cubic or tetragonal symmetry [35]. The Hamiltonian has the form

$$\hat{H} = -t_{\text{hop}} \sum_{\langle i,j\rangle} \sum_{\alpha\sigma} (c^\dagger_{i\alpha\sigma} c_{j\alpha\sigma} + c^\dagger_{j\alpha\sigma} c_{i\alpha\sigma}) + \sum_i \hat{H}_{\text{loc},i} - \mu \sum_{i\alpha\sigma} \hat{n}_{i\alpha\sigma}, \tag{1}$$

where $c^\dagger_{j\alpha\sigma}$ creates an electron on site i in orbital $\alpha = 1, 2$ with spin $\sigma = \uparrow, \downarrow$, $\hat{n}_{i\alpha\sigma}$ is the density operator $\hat{n}_{i\alpha\sigma} \equiv c^\dagger_{i\alpha\sigma} c_{i\alpha\sigma}$, t_{hop} is the nearest-neighbor hopping, $\hat{H}_{\text{loc},i}$ is the local interaction Hamiltonian on site i, and μ is the chemical potential. The interaction $\hat{H}_{\text{loc},i}$ has the general structure

$$\hat{H}_{\text{loc},i} = U \sum_\alpha \hat{n}_{i\alpha\uparrow}\hat{n}_{i\alpha\downarrow} + \sum_{\alpha\neq\beta} \sum_{\sigma,\sigma'} (U' - J\delta_{\sigma\sigma'}) \hat{n}_{i\alpha\sigma}\hat{n}_{i\beta\sigma'} + \gamma J \sum_{\alpha\neq\beta} (c^\dagger_{i\alpha\uparrow} c^\dagger_{i\alpha\downarrow} c_{i\beta\downarrow} c_{i\beta\uparrow} + c^\dagger_{i\alpha\uparrow} c^\dagger_{i\beta\downarrow} c_{i\alpha\downarrow} c_{i\beta\uparrow}), \tag{2}$$

where U is the intraorbital Coulomb interaction, U' is the interorbital Coulomb interaction, and J is the Hund's coupling. The interaction in Eq. (2) is the well-known Kanamori interaction [36], which becomes rotationally invariant when $U' = U - 2J$ and $\gamma = 1$.

Here, we set $U' = U - 2J$ but employ the nonsymmetric form (with $\gamma = 0$) for practical reasons. This approximation, which only retains the density-density interactions, has been shown to have a richer phase diagram than the isotropic model [37,38]. The lattice is assumed to be bipartite, and the noninteracting dispersion is chosen to yield a semicircular density of states with bandwidth $W = 4t_{\text{hop}}$. In the following, we use t_{hop} as the unit of energy, so that time is measured in units of $\hbar/t_{\text{hop}}$. The chemical potential is fixed to $\mu = (3U - 5J)/2$, which yields half-filling (two electrons per site). The system undergoes an antiferromagnetic spontaneous symmetry breaking at low temperature [37,38], but in the present study, we restrict our attention to the paramagnetic high-temperature Mott phase.

III. METHOD

To investigate the nonequilibrium dynamics of the two-band Hubbard model [Eq. (1)] in the strongly correlated paramagnetic Mott insulating phase, we employ real-time dynamical mean-field theory (DMFT) [17]. The DMFT formalism neglects the momentum dependence of the self-energy, i.e., $\Sigma(\mathbf{k},t;\mathbf{k}',t') \approx \Sigma(t,t')$, which allows to map Eq. (1) to an impurity action

$$S = \int_{\mathcal{C}} dt\, \hat{H}_{\mathrm{loc}}(t) + \iint_{\mathcal{C}} dt dt' \sum_{\alpha\sigma} c^{\dagger}_{\alpha\sigma}(t)\Delta_{\alpha\sigma}(t,t')c_{\alpha\sigma}(t') \tag{3}$$

with a self-consistently determined dynamical mean field in the form of a two-time-dependent hybridization function $\Delta_{\alpha\sigma}(t,t')$. The featureless semicircular density of states allows us to capture the general physics of the Mott insulator, and yields the simple self-consistency relation $\Delta_{\alpha\sigma} = t_{\mathrm{hop}}^2 g_{\alpha\sigma}$, where $g_{\alpha\sigma}$ is the impurity single-particle Green's function, $g_{\alpha\sigma}(t,t') \equiv -i\langle \mathcal{T} c_{\alpha\sigma}(t) c^{\dagger}_{\alpha\sigma}(t')\rangle_S$.

Since the Mott insulator is out-of-reach for weak coupling DMFT approaches [39,40] and variational approaches [41–47], we employ a pseudoparticle strong coupling (PPSC) real-time impurity solver. Introducing pseudoparticles enables diagrammatic expansion in the hybridization function, and we employ the first- and second-order self-consistent dressed approximation, also known as the noncrossing approximation (NCA) and one-crossing approximation (OCA) [48]. Since the dressed self-energy approximation can be written as a functional derivative of a (pseudoparticle) Luttinger-Ward functional [49,50], the PPSC expansion yields conserving approximations for both density and energy. These conservation laws are central for studying the time evolution of the system, especially at longer times. A detailed description of the method can be found in Ref. [48].

We have recently extended our real-time PPSC solver to general multiorbital systems, using both the blocking of the local Hamiltonian and a symmetry analysis of the pseudo particle diagrams to reduce the computational effort. The numerical symmetry analysis is flexible enough to automatically identify special situations such as spin and particle-hole symmetry, which for the paramagnetic half-filled two-band Hubbard model [Eq. (1)] with density-density interactions reduces the number of pseudoparticle NCA self-energy diagrams from 64 to 10, and the number of NCA single-particle Green's function diagrams from 32 to 12, for details see Appendix B.

Real-time DMFT directly gives the local single-particle Green's function $g_{\alpha\sigma}(t,t')$ of the system and the local many-body density matrix $\rho(t)$ through the pseudoparticle Green's function $\hat{G}(t,t')$, $\rho(t) = -i\hat{G}^{<}(t,t)$. In the case of density-density interaction, both $\hat{G}$ and ρ are diagonal in the local occupation number basis Γ, i.e., $\rho_{\Gamma\Gamma'} = \delta_{\Gamma\Gamma'}\rho_{\Gamma}$. Note that the trace over the local many-body density matrix is a conserved quantity, i.e.,

$$\sum_{\Gamma} \rho_{\Gamma}(t) = 1 \;\Rightarrow\; \sum_{\Gamma} \partial_t \rho_{\Gamma}(t) = 0. \tag{4}$$

The total energy of the system E_{tot} is the sum of the interaction (E_{int}) and kinetic (E_{kin}) energy, $E_{\mathrm{tot}} = E_{\mathrm{int}} + E_{\mathrm{kin}}$. Using the local multiplet energies E_{Γ}, E_{int} is obtained as

$$E_{\mathrm{int}}(t) = \sum_{\Gamma} \rho_{\Gamma}(t) E_{\Gamma}, \tag{5}$$

and E_{kin} is given by the equal-time contour convolution between Δ and g, $E_{\mathrm{kin}}(t) = -i\sum_{\alpha\sigma}[\Delta_{\alpha} * g_{\alpha\sigma}]^{<}(t,t)$, see Ref. [17].

The time evolution is solved using a fifth-order multistep method [51], and equidistant steps $\Delta t = 0.01 t_{\mathrm{hop}}$ in real time and $N_{\tau} = 100$ to 800 steps in imaginary time τ, $\tau \in [0,\beta)$, where β is the inverse temperature $\beta = 1/T$ [52]. The DMFT+PPSC approach is inherently memory bound since it employs two-time Green's functions [53] and we find that this typically limits the number of time steps N_t to $N_t \sim 1000$. The discretization errors are controlled by ensuring that the drift in the total density per site is below 10^{-4}. We note that the density conservation is sensitive to both real and imaginary time discretizations and therefore gives a good measure of the total convergence.

IV. RESULTS

A. Equilibrium

The equilibrium properties of the Mott phase in the strongly interacting half-filled two-band Hubbard model [Eq. (1)] are well understood within DMFT [54–62]. In what follows, we fix the interaction to $U = 15$ and the bandwidth to $W = 4$, which corresponds to the deep Mott-insulating regime, $U \gg W$. In equilibrium, a numerically exact DMFT solution can be obtained using the continuous time quantum Monte Carlo (CT-QMC) method [56,63,64], which allows to gauge the accuracy of our PPSC approach in the strong coupling regime.

In Fig. 2(a), we compare the equilibrium CT-QMC solution for the local single-particle Green's function $g_{\alpha\sigma}(\tau)$ in imaginary time τ, obtained using the hybridization expansion as implemented in the TRIQS application CTHYB [65–67], with the NCA and OCA results at inverse temperature $\beta = 1$ and relative Hund's coupling $J/U = 0.06$. We see that the strong local interaction ($U = 15$) makes the first-order strong coupling approximation (NCA) an extremely good approximation. The deviation between the Green's function obtained from NCA/OCA and CT-QMC is lower than the stochastic QMC noise $|g_{\mathrm{NCA/OCA}}(\tau) - g_{\mathrm{QMC}}(\tau)| < 0.004$ for $\beta = 1$ (and $\beta = 10$, not shown). Comparing NCA and OCA, we find that in contrast to the metallic single band case [48],

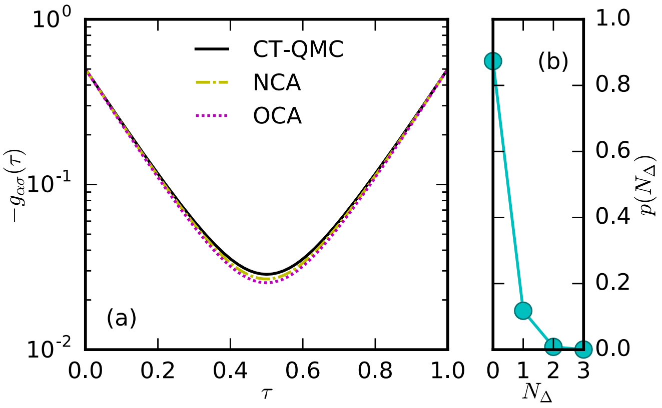

FIG. 2. (a) Equilibrium imaginary time single particle Green's function $g_{\alpha\sigma}(\tau)$ for $\beta = 1$, $U = 15$, and $J/U = 0.06$. Comparing exact continuous-time quantum Monte Carlo (CT-QMC) with first (NCA) and second-order (OCA) strong coupling expansions. (b) CT-QMC hybridization expansion probability contribution $p(N_\Delta)$ to the partition function (N_Δ is the perturbation order).

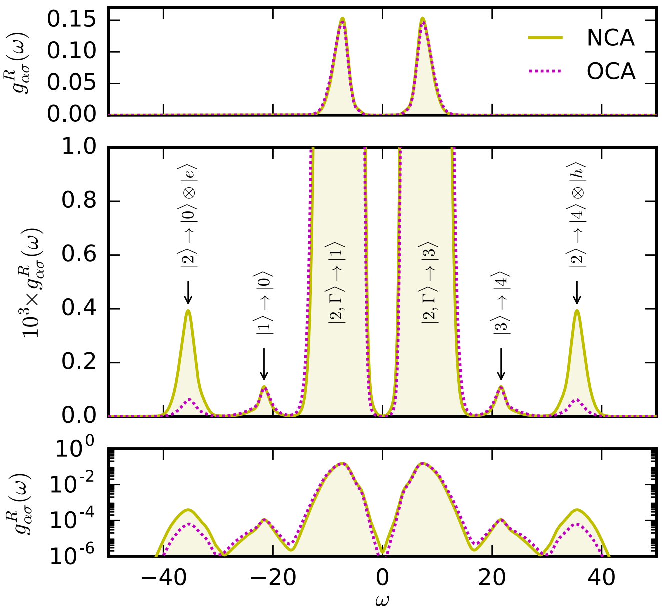

FIG. 3. Real-frequency equilibrium spectral function for $\beta = 1$, $U = 15$, and $J/U = 0.06$.

the OCA result is more correlated than the NCA result, i.e., $g_{\mathrm{OCA}}(\beta/2) < g_{\mathrm{NCA}}(\beta/2)$.

The good performance of NCA can be understood by looking at the distribution over hybridization perturbation orders in the CT-QMC solution, see Fig. 2(b). In the deep Mott state, the expansion of the partition function is dominated by the zeroth-order perturbation order $N_\Delta = 0$ (the atomic limit) with a ∼10% contribution from the first-order terms $p(N_\Delta = 1) \approx 0.1$, corresponding to a single hybridization insertion, while the second-order terms contribute less than one percent $p(N_\delta = 2) \lesssim 0.008$. The zeroth- and first-order contributions are exactly captured within NCA, and the higher-order contributions are exponentially small, hence the close agreement with CT-QMC.

By time evolving the equilibrium solution within NCA and OCA, we can directly obtain the real-frequency single-particle spectral function by Fourier transforming the real-time Green's function, see Fig. 3. The dominant spectral features of the half-filled Mott insulator are the lower and upper Hubbard bands centered around $\omega \approx \pm U/2 = \pm 7.5$. The single-particle spectral function corresponds to particle addition and particle removal for positive and negative frequencies ω, respectively. Thus the upper (lower) Hubbard band corresponds to the particle addition (removal) processes $|2,\Gamma\rangle \to |3\rangle$ ($|1\rangle$), where Γ is one of the doublon states listed in Fig. 1. In contrast to the single-band Hubbard model, the larger Hilbert space of the two-band model results in two additional spectral features at energies beyond the Hubbard bands. These resonances come in two classes, thermally activated and quantum fluctuation driven, analogous to what has previously been discussed for the Bose-Hubbard model [68]. The first resonance beyond the Hubbard bands arises from thermally activated electron-hole pair excitations in the ground state, which on particle addition (removal) produces the local transitions $|3\rangle \to |4\rangle$ ($|1\rangle \to |0\rangle$). While these resonances involve only the multiplet states at one site, the second resonance corresponds to concomitant addition (removal) of an electron and the emission of a hole $|h\rangle$ (particle $|p\rangle$) excitation into other lattice sites, i.e., $|2,\Gamma\rangle \to |4\rangle \otimes |h\rangle$ ($|2,\Gamma\rangle \to |0\rangle \otimes |p\rangle$). As seen in Fig. 3, NCA overestimates the spectral weight of the second resonance in comparison to OCA. However, since this resonance is very high in energy, its influence on the photodoping dynamics across the Hubbard gap is negligible. Hence, we will apply NCA in the study of the photodoping dynamics of the deep Mott insulator in what follows.

B. Nonequilibrium photodoping

To study the response of the two-band Mott insulator relevant to pump-probe experiments [69–71], we use a simplified driving to produce particle-hole transitions across the Mott gap (process I in Fig. 1). Specifically, we employ a two-cycle modulation of the single particle hopping with frequency $\Omega_{\mathrm{pump}} = 2.25U$ and a Gaussian envelope. This mechanism is different from the application of an electric field, but since we aim at investigating the relaxation *after* the excitation, the precise mechanism of generating carriers is not important, as long as it produces an essentially instantaneous excitation of particle-hole pairs across the Mott gap.

We focus again on the strongly correlated Mott insulator with Hubbard $U = 15$ and a single particle bandwidth fixed to $W = 4$. The recombination rate of triplons and singlons is in this case exponentially suppressed by the large Mott gap ($U \gg W$) [21,72,73] and the photodoping generated by the pump excitation is therefore an approximately conserved quantity on the numerically accessible time scales. In addition, to enable a direct comparison between systems with different strengths of the Hund's coupling J, we fix the density of photodoping induced singlon-triplon carriers after the pump to 1% by tuning the pump amplitude.

The system responds to the pump-excitation on all the time scales corresponding to characteristic energies of the Hamiltonian [Eq. (1)], i.e., (i) the Hubbard $U = 15$, (ii) the single particle hopping bandwidth $W = 4$, and (iii) the Hund's coupling $J \lesssim 0.05U = 0.75$. However, before we disentangle the photodoping dynamics in terms of the kinetic energy and the local many-body state occupations, we present results for the time-dependent photo emission spectra.

1. *Time-dependent photoemission spectroscopy*

To show how multiorbital and Hund's physics may be detected experimentally using time-dependent photoemission spectroscopy (TD-PES) [12,18], we study the time evolution of the nonequilibrium single-particle spectral function after the pump. Disregarding matrix elements and the finite width of the probe pulse this corresponds to the theoretical time-dependent photoemission spectrum [74]. The photodoping generates a redistribution of the spectral weight in both the retarded spectral function $g^R(\omega,t)$ and the lesser spectral function $g^<(\omega,t)$ defined as

$$g^\gamma(\omega,t) = \pm\frac{1}{\pi}\mathrm{Im}\int_t^\infty d\bar{t}\, e^{-i(\bar{t}-t)\omega} g^\gamma(t,\bar{t}), \qquad (6)$$

where ω is the relative frequency, t is the absolute time, the $+(-)$ sign corresponds to the lesser, $\gamma =<$ (retarded, $\gamma = R$) component.

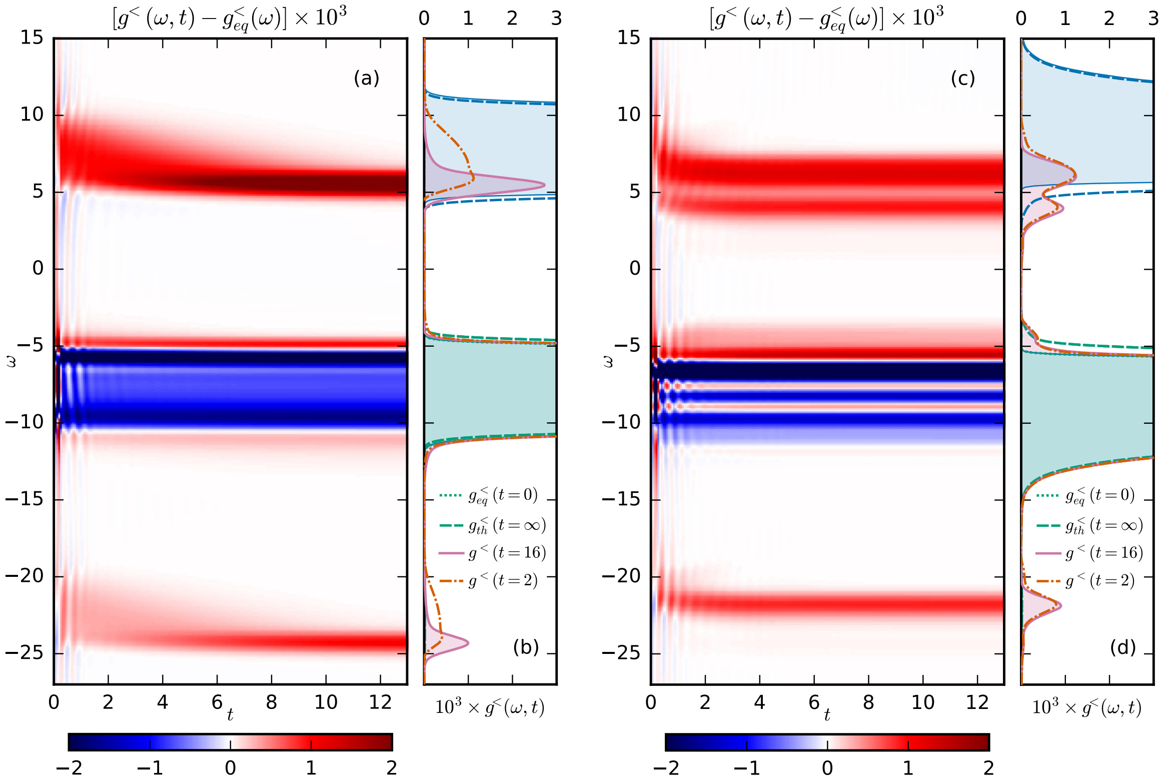

FIG. 4. Theoretical time-dependent photoemission spectra showing the kinetic energy relaxation of the photodoped triplons in the upper Hubbard band for $U = 15$, $T = 0.1$, $J/U = 0.01$ [(a) and (b)], and $J/U = 0.06$ [(c) and (d)].

Since the lesser spectral function $g^<(\omega,t)$—i.e., the occupied density of states (DOS)—is the main observable in TD-PES, we focus on the time-dependent change in $g^<(\omega,t)$ relative to the time-translational invariant occupied DOS $g^<_{\mathrm{eq}}(\omega)$ of the initial equilibrium state. In Fig. 4, the differential response of the occupied DOS is shown for $J/U = 0.01$ [Figs. 4(a) and 4(b)] and $J/U = 0.06$ [Figs. 4(c) and 4(d)].

The short pulse injects particle-hole pairs (singlon-triplon pairs) with high kinetic energy into the Hubbard bands (process I in Fig. 1), and thus results in an initial spectral weight redistribution from the lower to the upper Hubbard band. The singlons and triplons then relax their high kinetic energy by emitting doublon spin excitations (processes IIa and IIb in Fig. 1) when scattering off the high spin doublon background, as indicated in the upper Hubbard band in Fig. 1. The result is a drift of the occupied density of states in the upper Hubbard band from the upper band edge to the lower band edge. However, as can be seen by comparing Figs. 4(a) and 4(b) with 4(c) and 4(d) the relaxation dynamics and the spectral features induced by this cooling process depend strongly on the Hund's coupling J.

At small Hund's coupling, e.g., $J/U = 0.01$ as in Figs. 4(a) and 4(b), the kinetic relaxation of triplons manifests itself primarily as a redistribution of occupied spectral weight within the upper Hubbard band. A short time after the pulse [see $t = 2$ dot-dashed curve in Fig. 4(b)] the broad distribution in the upper Hubbard band indicates the presence of triplons with high kinetic energy. This population relaxes at later times to a thermal-like distribution (solid red line), albeit with a shifted chemical potential. While the triplons apparently "thermalize" within the upper Hubbard band, the large Mott gap exponentially suppresses singlon-triplon recombination, which is required for the system to reach a true thermal equilibrium state.

The observed population dynamics within the Hubbard band [Figs. 4(a) and 4(b)] is similar to the dynamics of photodoped antiferromagnetic systems [31,32] or systems coupled to lattice degrees of freedom [26,30,75], where the electrons interact with external bosonic degrees of freedom. Thus, at weak Hund's coupling, the local doublon spin degrees of freedom in the two band model qualitatively act as a boson bath into which the electronic degrees of freedom can transfer excess kinetic energy.

We also note that the dynamics in the Hubbard band is reproduced in the second Hubbard resonance at $\omega \approx -3U/2 = -22.5$, see Figs. 4(a) and 4(b). This spectral feature corresponds to the particle removal transition $|1\rangle \rightarrow |0\rangle$, as previously discussed in Fig. 3. Note that the singlon population (corresponding to the unoccupied DOS) in the lower Hubbard band is the mirror copy of the triplon population in the upper Hubbard band, by particle-hole symmetry (not shown). Hence, while triplons relax towards lower frequencies at the lower band edge of the upper Hubbard band, singlons relax towards higher (small negative) frequencies at the upper band edge of the lower Hubbard band. In contrast, the resonance $|1\rangle \rightarrow |0\rangle$ at $\omega \approx -22.5$ in the occupied density of state represents photoemission from a singlon state, and displays a reversed relaxation towards low (large negative) frequencies. Since the multiplet energy separation between the singlon and holon state is equal to U the singlons at the upper band edge of the

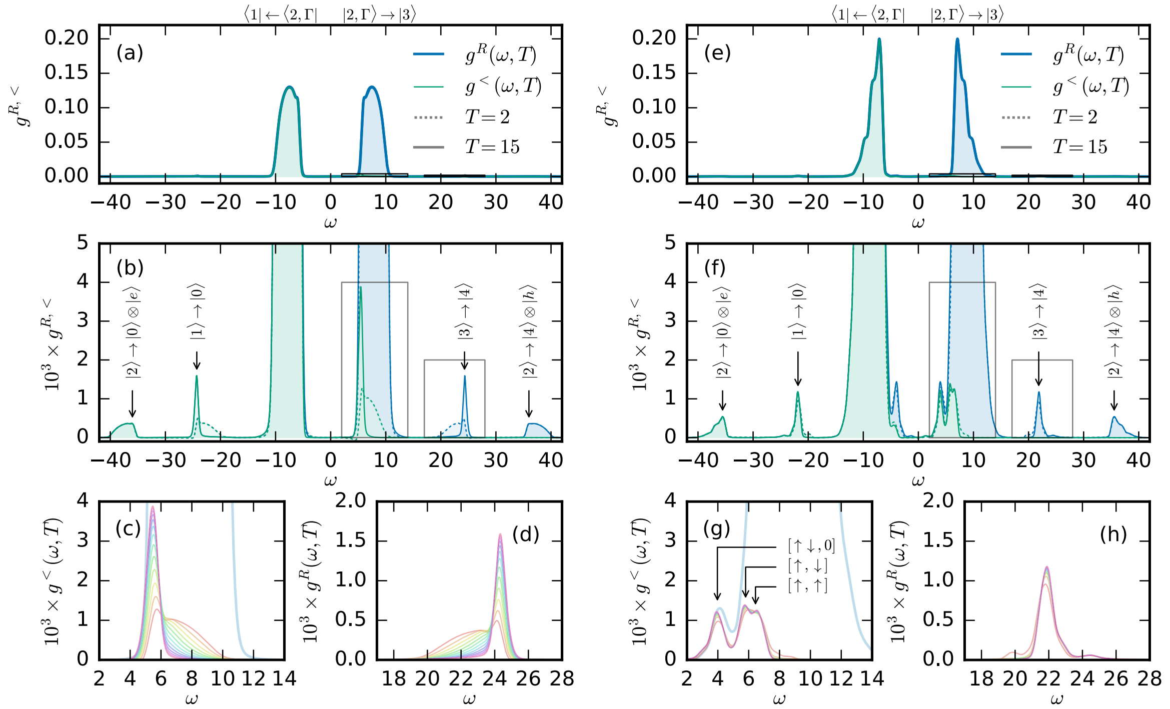

FIG. 5. Time-evolution of the single-particle retarded Green's function $g^R(\omega,T)$ (blue) and lesser Green's function $g^<(\omega,T)$ (green), for $U = 15$, $\beta = 10$, $J/U = 0.01$ [(a)–(d)], and $J/U = 0.06$ [(e)–(h)]. (c), (d), (g) and (h) show all integer times $t = 2$ to 14 (red to blue).

lower Hubbard band with large (small negative) kinetic energy require a smaller excitation energy in the $|1\rangle \rightarrow |0\rangle$ transition, whence these singlons produce the low-frequency structure in the $\omega = -3U/2$ resonance.

While this spectral feature is present in equilibrium at elevated temperatures due to thermal activation of singlon states (Fig. 3), its emergence after the pump is a nonequilibrium effect induced by the photodoped singlons. We note that the emergence of satellites below the lower Hubbard band is a generic feature of multiorbital systems with Hubbard U interaction, due to the additional states in the local Fock space with higher/lower occupation numbers. The generation of this class of side bands in photodoped multiorbital systems could be used to experimentally detect the presence of multiorbital interactions in an out-of-equilibrium setup.

For larger J/U, the time scale of the kinetic relaxation becomes shorter, and for $J/U = 0.06$ the initial high to low kinetic energy triplon redistribution overlaps with the short-lived coherent $2\pi/U$ oscillations at $t \lesssim 2$, see Figs. 4(c) and 4(d). In this regime, the relaxation changes its qualitative behavior. After the fast kinetic relaxation, the occupied spectral weight in the upper Hubbard band no longer comprises a single resonance, instead, the spectral weight is split into two main resonances (at $\omega \approx 4$ and $\omega \approx 7$), see Fig. 4(d). Furthermore, the second Hubbard resonance (at $\omega = -22$) is no longer a mirror copy of the entire occupied spectral weight in the upper Hubbard-band, but rather only a mirror copy of the low-energy resonance.

The splitting of the occupied spectral weight in the upper Hubbard band of Figs. 4(c) and 4(d) can be understood in terms of the Hund's coupling induced splitting of the doublon states, where the $S = 0$ doublon states $[\uparrow,\downarrow]$ and $[\uparrow\downarrow,0]$ (see Fig. 1) are split off from the high-spin $S = 1$ doublon states $[\uparrow,\uparrow]$ by J and $3J$, respectively. After the pump excitation, the excess triplon density can transition to all three doublon states on particle removal, which directly produces three resonances in the upper Hubbard band, corresponding to the processes $|3\rangle \rightarrow |2,\Gamma\rangle$, while only two resonances are discernible in Figs. 4(c) and 4(d) (due to limited frequency resolution) the stronger resonance consists of two peaks, see Fig. 5(g). Note that the particle-hole symmetric process $|1\rangle \rightarrow |2,\Gamma\rangle$ produces a shoulder feature at the upper edge of the lower Hubbard band, at $\omega \approx -5$ in Fig. 4(d), which might be simpler to detect experimentally than the occupied DOS in the upper Hubbard band. We propose that the detection of a splitting of the photodoped occupation in the upper Hubbard band and the emergence of a low-energy shoulder of the lower Hubbard band can serve as a "litmus test" for strong Hund's coupling in Mott insulators.

A similar reasoning also explains why the second Hubbard resonance (at $\omega \approx -23$) only displays a single peak, see Figs. 4(c) and 4(d). This spectral feature corresponds to the removal of a photodoping induced singlon state, i.e., $|1\rangle \rightarrow |0\rangle$. Since these states are not split by the Hund's coupling J the transition only yields a single peak.

So far, we have focused on the occupied density of states since it is experimentally observable in TD-PES. However, our real-time DMFT calculations give direct access also to the retarded spectral function $g^R(\omega,t)$. Thus we are able to give the complete picture of the spectral distribution throughout the relaxation, see Fig. 5. Beyond the features already identified in the differential TD-PES, the full spectral function shows the general shape of the Hubbard bands at $J/U = 0.01$ and 0.06, see Figs. 5(a) and 5(e). Going from low to high J, the Hubbard bands develop from a resonance with a low-frequency shoulder, into a resonance with two shoulders on the high-frequency side. In addition, Figs. 5(b) and 5(f) show not only the redistribution due to kinetic relaxation but also that the third resonances beyond the upper and lower Hubbard bands (at $|\omega| \approx 36$) are not affected by the pump excitation. This can be understood by considering the local transitions that give rise to the resonance, e.g., at positive frequencies they correspond to $|2,\Gamma\rangle \to |4\rangle \otimes |h\rangle$ (where $|h\rangle$ is an emitted hole on the lattice). Since the singlon-triplon states are not directly involved in these transitions, their relaxation does not affect this third class of resonances.

Detailed plots of time slices at the upper Hubbard band and the second resonance clearly show that at low $J/U = 0.01$, they are mirror copies of each other, see Figs. 5(c) and 5(d). At this low Hund's coupling, the thermal activation in the initial state with $T = 0.1$ makes it impossible to resolve the individual doublon excitations since their splitting $J = 0.15$ is of the same order, $J \approx T$. At larger Hund's coupling $J/U = 0.06$, however, the splitting of the atomic multiplets gives rise to a separation of the occupied DOS in the upper Hubbard band, see Figs. 5(f) and 5(g). In this particular case, all three resonances are resolved in Fig. 5(f) [due to better spectral resolution as compared to Fig. 4(d)]. We also note that the shoulder feature in the lower Hubbard band is even more pronounced in the retarded spectral function at $\omega \approx -5$ as compared to the feature in the occupied DOS, cf. green and blue lines in Fig. 5(f). Further, while the second resonance qualitatively is a single peak [see Fig. 5(h)], a close inspection reveals additional structures. In particular, it has a high-energy extended shoulder feature due to higher-order processes.

2. *Short-time particle-hole excitations*

In order to understand the photocarrier relaxation observed in our time-dependent PES results, in particular its dependence on the relative Hund's coupling J/U and temperature T, we perform a detailed analysis of the relaxation dynamics. To do this, we will exploit the fact that our PPSC method also provides information about the local many-body density matrix $\rho(t)$, and use this to study the time evolution of the different local many-body states throughout the relaxation process as a function of T and J/U.

The short-time response of the system at $t \lesssim 2$, shown in Fig. 6, displays only the two fastest time scales U and W. The response during the application of the pump (gray line) is dominated by a rapid increase of the singlon and triplon probability $\rho_1 = \rho_3$, with a concomitant reduction of all doublon probabilities $\rho_{2,\Gamma}$ due to Eq. (4). The sudden increase is followed by a damped oscillatory decay, see Fig. 6. The corresponding photodoping ρ_d is defined as the combined change in singlon-triplon probability $\Delta\rho_{1,3}(t) = \rho_{1,3}(t) - \rho_{1,3}(0)$ and holon-quadruplon probability $\Delta\rho_{0,4}(t) = \rho_{0,4}(t) - \rho_{0,4}(0)$, i.e., $\rho_d \equiv \Delta\rho_{1,3}(t) + \Delta\rho_{0,4}(t)$. However, since the density of holon-quadruplon high-energy excitations is negligible, $\Delta\rho_{0,4}(t) \approx 0$. Except at very high initial temperature ρ_d effectively measures the singlon-triplon doping $\rho_d \approx \Delta\rho_{1,3}$. The oscillation frequency $\Omega_{1,3}$ is approximately equal to the Hubbard-U, $\Omega_{1,3} \sim U$, and the inverse relaxation time $\tau_{1,3}^{-1}$ is of the order of the bandwidth, $\tau_{1,3}^{-1} \approx W$. Both frequency and damping are only weakly dependent on the Hund's coupling J, since the corresponding time scale is long, see the lower panel in Fig. 6.

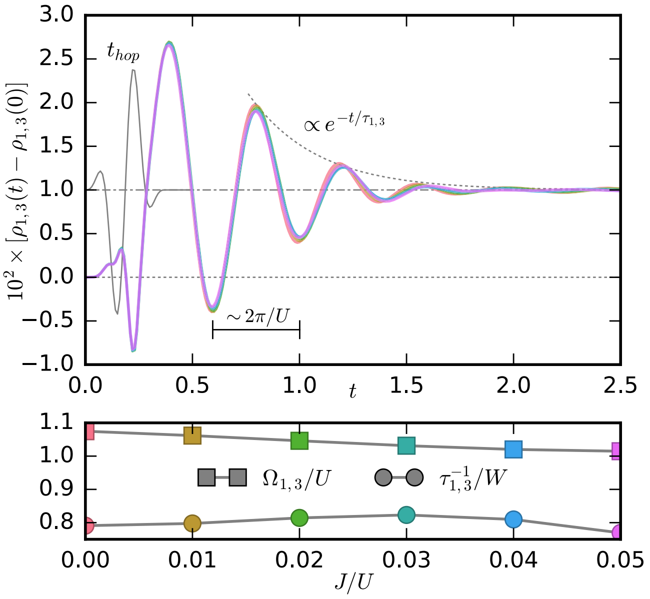

FIG. 6. Short-time dependence of the photodoping pump-induced change in the singlon-triplon density $\rho_{1,3}(t) - \rho_{1,3}(0)$ for $U = 15$, $\beta = 1$, and $J/U = 0.00$ to 0.05 (upper panel), showing damped $2\pi/U$ oscillations $\Omega_{1,3} \sim U$ with an inverse relaxation time $\tau_{1,3}^{-1}$ of the order of the bandwidth W (bottom). The hopping modulation $t_{\text{hop}}(t)$ of the pump pulse is shown as a gray thin solid line in the upper panel.

The time evolution of the system's energy components—in the same time window—is shown in Figs. 7(a) and 7(b). The hopping modulation of the pump only lasts for $t \lesssim 0.5$ and concomitantly the total energy E_{tot} of the system displays an oscillatory increase [Fig. 7(a)]. After the pulse the total energy E_{tot} again becomes a conserved quantity, $\partial_t E_{\text{tot}}(t) = 0$ for $t \gtrsim 0.5$. The increase of the photodoping yields an increase in the local interaction energy E_{int}. The oscillatory behavior with frequency $\Omega_{1,3} \sim U$ is driven by a shuffling between singlon-triplon interaction energy $E_{1,3}$ and kinetic energy E_{kin} at times $t \lesssim 2$, as shown in Fig. 7(b).

The photodoping (i.e., the change in the singlon-triplon probability density $\Delta\rho_{1,3}$) only becomes an approximately conserved quantity after the $2\pi/U$ oscillations have damped out at times $t \gtrsim 2$. The short-time behavior and photodoping conservation is similar to the dynamics seen in the single-band Hubbard model. However, at longer times, the (paramagnetic) single-band and two-band models exhibit different relaxation dynamics.

While both the photoexcited single-band and two-band models are (in the large-U limit) trapped in a long-lived nonthermal state, since the recombination of particle-hole pairs is exponentially suppressed by the Mott gap [19,20], the evolution of the photodoped population within the Hubbard bands is very different. In the single-band case, the redistribution of spectral weight (and the associated relaxation of the kinetic energy) is very slow [20]. In contrast, as shown in Fig. 1 and discussed in Sec. IV B 1, the photodoped population can quickly relax within the Hubbard bands due to the additional

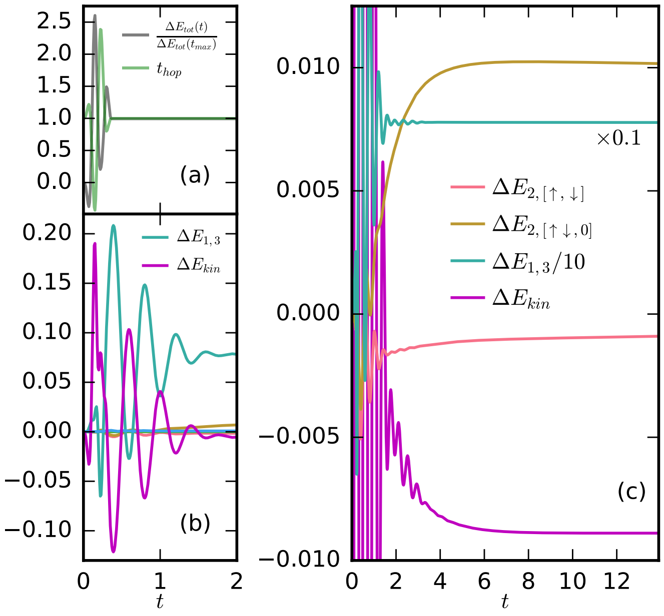

FIG. 7. Three stages of excitation/relaxation: (a) hopping modulation t_{hop} (green) and increase of the total energy E_{tot} (black) at $t \lesssim 0.5$, (b) energy conversion between kinetic energy E_{kin} (magenta) and singlon-triplon interaction energy $E_{1,3}$ (blue) at $t \lesssim 2$ (cf. Fig. 6), and (c) conversion from (singlon-triplon) kinetic energy to interaction energy in terms of $S = 0$ doublon excitations $E_{2,[\uparrow,\downarrow]}$ (red) and $E_{2,[\uparrow\downarrow,0]}$ (yellow), cf. (IIa) and (IIb) in Fig. 1. The approximately conserved singlon-triplon energy $\Delta E_{1,3}$ (rescaled by 0.1) is also shown (blue).

orbital degrees of freedom and the local spin excitations generated by the Hund's coupling J energy scale.

If we would consider an antiferromagnetically ordered system, then even the single-band Hubbard model would show a similar kinetic energy relaxation [24], whose relaxation rate would be determined by the exchange energy scale J_{ex}, which is different from the Hund's coupling J that controls the cooling dynamics of the (paramagnetic) two-orbital system. While we will not consider the interplay of the two scattering processes in the antiferromagnetically ordered two-orbital case in this work, it is clear that the J_{ex}-based relaxation mechanism will depend strongly on temperature and (within single-site DMFT) will disappear above the Neel temperature, while the Hund's-J based mechanism will persist above this temperature, provided that $J > J_{\text{ex}}$. Since the flipping of $S = 1$ moments requires four hoppings, we generically expect that the Hund's coupling mechanism indeed dominates.

3. Doublon excitations

The photodoped two-band Mott-insulator with finite Hund's coupling $|J| > 0$ has, due to the lifted doublon degeneracy, internal degrees of freedom in the doublon subsector. The approximate conservation of the photoexcited singlon-triplon density $\rho_{1,3}(t)$ and holon-quadruplon density $\rho_{0,4}(t)$, i.e.,

$$\partial_t \rho_{1,3}(t) \approx 0, \quad \partial_t \rho_{0,4}(t) \approx 0 \tag{7}$$

implies that the conservation of total local probability [Eq. (4)] constrains the probabilities of the three inequivalent doublon states,

$$\partial_t \rho_{2,[\uparrow,\uparrow]} + \partial_t \rho_{2,[\uparrow,\downarrow]} + \partial_t \rho_{2,[\uparrow\downarrow,0]} \approx 0. \tag{8}$$

Note that each label is assumed to encompass all possible permutations and directions of spin, i.e., $[\uparrow,\uparrow]$ also includes $[\downarrow,\downarrow]$ and $[\uparrow,\downarrow]$ also includes $[\downarrow,\uparrow]$, etc.

From the energetic point of view the remaining degree of freedom is the conversion between kinetic energy E_{kin} and interaction energy in the doublon subsector $E_{\text{int},2}$, i.e., $\partial_t(E_{\text{kin}} + E_{\text{int},2}) \approx 0$, where $E_{\text{int},2}$ is given by the weighted sum of the occupation probabilities $\rho_{2,\Gamma}$ of the doublon states (with two electrons $N_e = 2$) and their atomic multiplet energies $E_{2,\Gamma}$:

$$E_{\text{int},2} = \sum_{\Gamma \in \{\Gamma : N_e = 2\}} \rho_\Gamma E_\Gamma, \tag{9}$$

cf. Eq. (5). The kinetic energy relaxation of the pump-generated singlon-triplon excitations by the production of doublon spin excitations, i.e., step (II) in the illustration of Fig. 1, can directly be seen in the time-evolution of the system's energy components at times $t \gtrsim 2$ in Fig. 7(c). The kinetic energy E_{kin} shows an exponential decrease, accompanied by a corresponding increase in the interaction energy for the high-energy $S = 0$ doublon state with local double occupancy $\Delta E_{2,[\uparrow\downarrow,0]}$, and a smaller and slower increase in the low-energy $S = 0$ doublon state interaction energy $\Delta E_{2,[\uparrow,\downarrow]}$. These two processes correspond to the scattering processes (IIa) and (IIb) in Fig. 1, respectively.

4. Temperature dependence

We find that the speed and magnitude of the response of the different energy components is very sensitive to both the Hund's coupling J and the temperature T of the initial state. Since the temperature dependence is experimentally accessible, we begin by investigating how the relaxation dynamics depends on T.

At low temperature $T \ll J$, the initial state is dominated by high spin doublons $[\uparrow,\uparrow]$ and singlon-triplon quantum fluctuations. In this regime the excited doublon states ($[\uparrow,\downarrow]$ and $[\uparrow\downarrow,0]$) are exponentially suppressed due to the Hund's coupling induced splitting of these states (J and $3J$, respectively).

To see this, we fix $J/U = 0.04$, i.e., $U = 15$ and $J = 0.6$, and sweep temperature from $T = 0.1$ to 2.5, see Fig. 8. At $T = 0.1$, the high-spin doublon (green circles) dominates the local many-body density matrix $\rho_{2,[\uparrow,\uparrow]} \lesssim 1$, while the occupations of the low-energy (red circles) and high-energy doublons (yellow circles) are exponentially suppressed. The low-energy doublon occupation $\rho_{2,[\uparrow,\downarrow]}$ (red), with an energy splitting of $J = 0.6$, rapidly grows when increasing the temperature T from 0.1 to 1, see Fig. 8(a), while the high-energy doublon density $\rho_{2,[\uparrow\downarrow,0]}$ (yellow) displays a slower increase, due to its larger energy splitting $3J = 1.8$.

We find that the 1% photo doping, i.e., the change in the singlon-triplon and holon-quadruplon occupation after the pump, $\rho_p = \Delta\rho_{1,3} + \Delta\rho_{0,4}$, does not drastically change the local multiplet occupations. As can be seen from the occupations

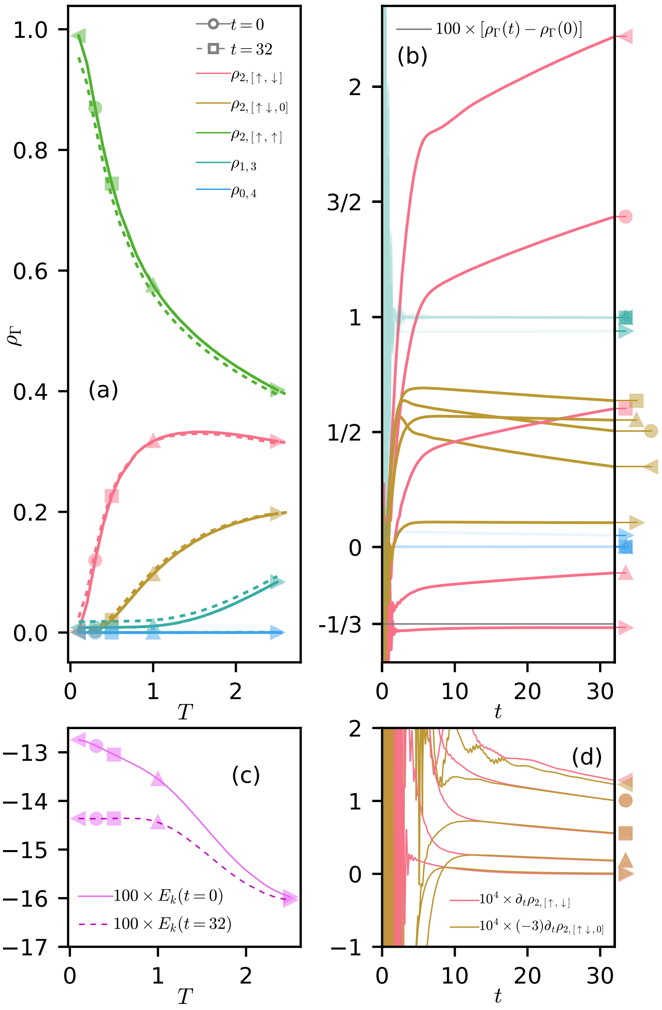

FIG. 8. (a) Local multiplet probabilities ρ_Γ at time $t = 0$ (solid lines) and at $t = 32$ after 1% photodoping (dashed lines) for a range of temperatures $T = 0.1$ to 2.5 with $W = 4$, $U = 15$, and $J/U = 0.04$, (b) their relative changes $\rho_\Gamma(t) - \rho_\Gamma(0)$ in time, showing the processes IIa (yellow) and IIb (red) of Fig. 1, (c) the kinetic energy E_k at $t = 0$ and $t = 32$, and (d) scaled time derivatives of the two doublon excitation multiplet densities. The shape of the markers indicates the temperature. In (b) and (d), real-time results for initial temperatures $T = 0.1$ (left triangles), 0.3 (circles), 0.5 (squares), 1.0 (up triangles), and 2.5 (right triangles) are shown.

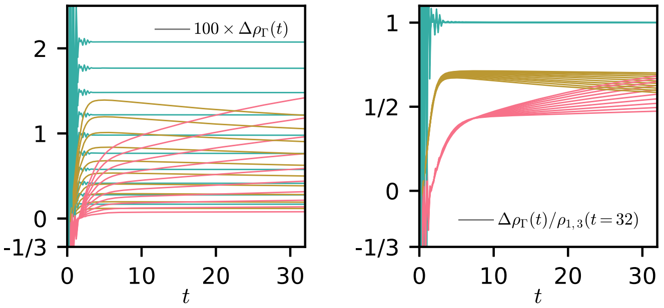

FIG. 9. Change in the local multiplet probability relative to the initial ground state, $\Delta\rho_\Gamma(t) \equiv \rho_\Gamma(t) - \rho_\Gamma(0)$, for several different photodoping densities (left). Rescaling with the long-time singlon-triplon photodoping density $\rho_{1,3}(t = 32)$ reveals more clearly the doping dependence of the low spin doublon (red and yellow) conversion rate (right). The color coding is defined in Fig. 8.

at time $t = 32$ after the pulse [dashed lines in Fig. 8(a)], the pump-induced redistribution in the doublon subsector is also of the order of one percent.

While the absolute changes in the probability distribution among the local multiplet states Γ are small, the time-dependent deviations from the initial state $\Delta\rho_\Gamma(t) \equiv \rho_\Gamma(t) - \rho_\Gamma(0)$ are nontrivial, see Fig. 8(b). Due to the large Mott gap and the induced conservation laws Eqs. (7) and (8) the three state dynamics in the doublon sector is captured by the occupation probabilities of the two excited doublons. The excited doublon densities (red and yellow) show an initial fast exponential rise followed by a slow near linear drift, see Fig. 8(b). The speed in the initial rise of the high-energy doublon (yellow) as compared to the low-energy one (red) correlates well with the difference in their multiplet energies (J and $3J$). Intriguingly, when extrapolating the exponential rise back to $t = 0$ (disregarding the $2\pi/U$ oscillations at short times), we find that all doublon densities extrapolate to a $-1/3\%$ absolute reduction as compared to the initial state. In other words, the 1% photodoping increase of the singlon-triplon and holon-quadruplon states by the high-frequency pulse results in a rapid and even reduction of $1/3\%$ of all three doublon states. This, however, requires all doublon states to be populated in the initial state, i.e., $J \lesssim T$.

The slower dynamics at times $t \gtrsim 5$ additionally conserves the local interaction and kinetic energy, which can be seen in the weighted time derivatives of the doublon occupations, see Fig. 8(d). Every high-energy doublon with energy $3J$ decays into three low-energy doublons with energy J by scattering of the high-spin doublon background. This conversion corresponds to the derivative matching: $\partial_t\rho_{2,[\uparrow,\downarrow]} \approx -3\partial_t\rho_{2,[\uparrow\downarrow,0]}$ shown in Fig. 8(d). The dominant decay channel for this energy conserving doublon conversion is, however, still mediated by the singlon-triplon photodoped carriers. Thus the doublon conversion rate is sensitive to the photodoping density, as shown in Fig. 9.

While the pump generates singlon-triplon pairs with high kinetic energy, the initial relaxation of the total kinetic energy occurs during the initial fast rise for $t \lesssim 5$ (not shown). The largest kinetic energy change (≈10%) occurs at low initial temperatures, see Fig. 8(c), and it is substantial considering the 1% fixed photodoping. At higher temperature the photoinduced kinetic energy change is reduced since the initial thermal state already populates the excited doublon sector. In fact, the thermal activation of the low-energy doublon results in a *thermal blocking* of its dynamics. This can be seen from the monotonic reduction of the low-energy doublon density (red) in Fig. 8(b). At low temperature, the dynamics is dominated by the low-energy doublon, but as temperature is increased its amplitude is rapidly suppressed [correlating with its thermal activation in the initial state, see Fig. 8(a)]. For temperatures $T > J = 0.8$, this reduction is so severe that the high-energy doublon (yellow) exhibits the largest response to the photodoping.

Interestingly, at $T = 2.5$, where the low-energy doublon is almost completely thermally blocked, the initial $-1/3\%$

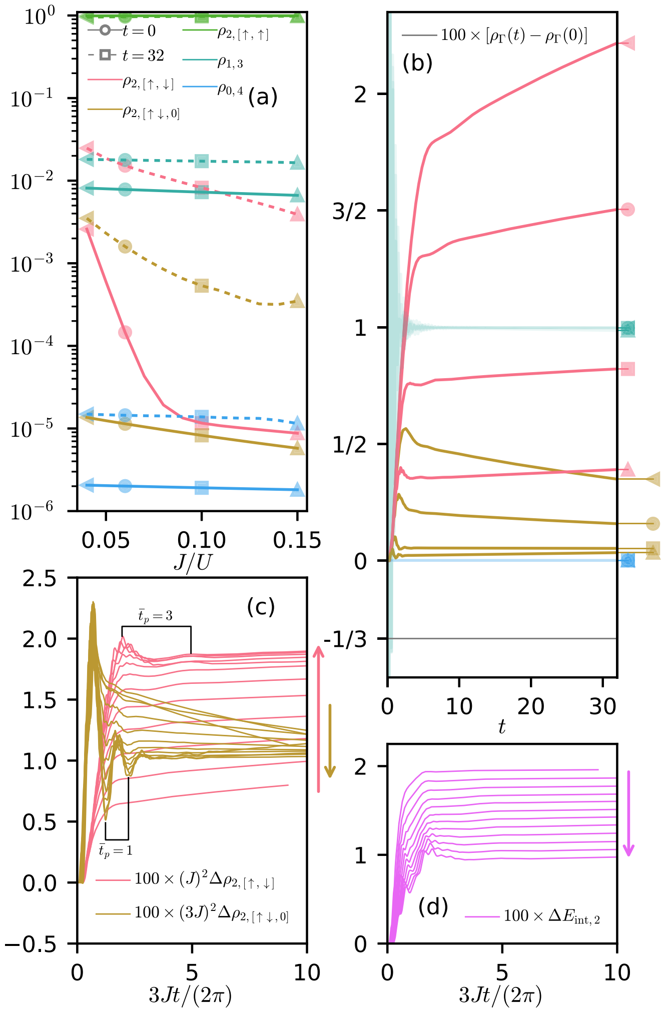

FIG. 10. (a) Local multiplet probabilities ρ_Γ at time $t = 0$ (solid lines) and at $t = 32$ after 1% photodoping (dashed lines) for a range of Hund's couplings $J/U = 0.04$ to 0.15 with $W = 4$, $U = 15$, and $\beta = 10$; (b) their relative changes $\rho_\Gamma(t) - \rho_\Gamma(0)$ in time, showing the processes IIa (yellow) and IIb (red) of Fig. 1 for $J/U = 0.04$ (left triangles), 0.06 (circles), 0.10 (squares), and 0.15 (up triangles); (c) rescaled time $2Jt/(2\pi)$ and magnitude $(E_\Gamma)^2\rho_{2,\Gamma}$ of the two doublon densities; and (d) total change of interaction energy in the doublon subsector $\Delta E_{\mathrm{int},2}$. The color-coded markers indicate the value of the Hund's coupling, and the arrows in (c) and (d) indicate the direction of increasing J/U.

offset still persist. This can be understood as an effect of a quasi instantaneous 1% photo doping change in the singlon-triplon density which by probability conservation [Eq. (4)] requires the doublon probability densities to be reduced by an equal amount (assuming that the excitation is below the holon-quadruplon threshold).

5. *Hund's coupling dependence*

We finally investigate the dependence of the photocarrier relaxation on the Hund's coupling in Fig. 10 at fixed $T = 0.1$. At this low initial temperature, the doublon excitations are suppressed, while the singlon-triplon fluctuations persist at almost one percent in the initial state, due to hopping driven quantum fluctuations. However, one can still see thermal activation effects of doublons at low J/U since in this limit $T \sim J$. For this reason, the low-energy doublon excitation (red solid line) displays a marked increase for $J/U \lesssim 0.08$, see Fig. 10(a).

The time dependence of the probability density changes in Fig. 10(b) show that the roles of the doublon states when tuning J/U are reversed, as compared to the increasing temperature. For higher J/U, the high-energy doublon state (yellow) is successively more suppressed, and the dynamics is instead dominated by the low-energy doublon (red). The suppression of the high-energy doublon can be understood by kinetic energy arguments. At $J/U \gtrsim 0.09$, the high-energy doublon splitting $3J$ exceeds the bandwidth $W = 4$ and high kinetic energy singlons and triplons can no longer excite these high-energy doublons. We coin this effect *kinetic freezing*. It acts in the opposite direction as compared to *thermal blocking*.

There is also an interesting structure in the short-time dynamics of the doublon excitations, which directly reveals their atomic-like properties. This manifests itself in the damped oscillations occurring directly after the initial fast rise. We find that this short-time dynamics exhibits a well defined scaling with respect to the Hund's coupling. The time and amplitude rescaling

$$t \to \frac{3J}{2\pi} t, \quad \Delta\rho_\Gamma \to (E_\Gamma)^2 \Delta\rho_\Gamma \tag{10}$$

approximately collapses the short-time doublon dynamics, see Fig. 10(c). This time rescaling reveals that the frequency Ω of the damped oscillatory response scales with Hund's J. The rescaled period $\bar{t}_p = 1$ for the high-energy doublon (yellow) in Fig. 10(c) corresponds to a frequency $\Omega = 3J$, while the period $\bar{t} = 3$ for the low-energy doublon (red) corresponds to a frequency $\Omega = J$. Thus the short-time response contains information on the multiplet splittings.

The amplitude scaling with the square of the multiplet energy $(E_\Gamma)^2 \propto J^2$ approximately collapses the probability densities for the high-energy doublon (yellow). However, the low-energy doublon dynamics (red) shows clear deviations [Fig. 10(c)]. This deviation from the J^2 scaling of the low-energy doublon occurs in the low J/U regime ($J/U < 0.08$), where it is thermally activated in the initial state, see Fig. 10(a).

After the initial short-time dynamics $t \lesssim 10$, the system still shows a conversion between doublon states, while the total interaction and kinetic energy is conserved, see Fig. 10(d). This is a direct analog to the temperature sweep results discussed previously. Interestingly, we find that the conversion between high and low-energy doublon excitations changes direction, when going from low to high J/U. While the high-energy doublon population indeed gets frozen when $3J > W$, at even higher J/U it starts to slowly grow with time. We speculate that this effect has to do with direct high-energy doublon to singlon-triplon transitions, since at $J/U = 0.2$ these two states become degenerate. In this regime, the system becomes unstable with respect to charge disproportionation [76], which should have profound effects on the nonequilibrium dynamics. However, since this requires rather high J/U that are not commonly found in real materials we do not study this regime here.

While the preceding analysis of the relaxation dynamics has been based on the single-particle spectral function and the local many-body density matrix, the pseudoparticle method provides a complementary view on the system's dynamics in terms of the pseudoparticle spectral functions. In particular, from this analysis, it is evident that the dominant contribution to the kinetic energy, and the kinetic energy relaxation, comes from the singlon-triplon states. For details see Appendix A.

V. DISCUSSION AND CONCLUSIONS

A series of recent theoretical studies has shown that already the single-band Hubbard model exhibits a nontrivial thermalization dynamics after photoexcitation [17–19], in particular an exponential dependence of the photocarrier lifetime with the Mott gap [19–21], impact ionization in the small gap regime $U \gtrsim W$ [22], and an unconventional nature of the photodoped metallic state [23]. Nonlocal interactions [26,33,34] and spin correlations [24,25] lead to qualitative changes in the relaxation dynamics of the photocarriers, as does the coupling to phonons [26–30].

The results of the present analysis show that local orbital degrees of freedom and Hund's coupling further enrich the response to photodoping in the strongly interacting Mott insulator, and lead to qualitatively new physics, which manifests itself in new features of the nonequilibrium spectral function and new relaxation time scales. This is central for the understanding of pump-probe experiments, since most correlated materials contain multiple orbitals in the vicinity of the Fermi level (typically a mix of transition metal d states and oxygen/pnictogen p orbitals) and cannot be represented by an effective single-band Hubbard model. Here, we focused on the case with strongly correlated orbitals only. The analysis of a photodoped state with weakly correlated holes and strongly correlated doublons, as realized for example in a d-p model of cuprates, is an interesting topic for a separate future study.

To highlight the qualitative differences between the single- and multiband systems, we have studied the dynamics of the paramagnetic half-filled two-band Hubbard model with local density-density interactions after a photodoping pulse. By analyzing the dynamics of the local many body states and the single-particle time-dependent photoemission spectra (TD-PES), we identified a number of qualitatively new features of multiorbital models. In particular, we observed additional side peaks in the occupied TD-PES spectra, and showed that these result from transitions between local states with one and two electrons less than the nominal filling. This is a general feature of multiorbital systems with several local occupation states. We also observed a splitting of the photodoped carrier population in the upper Hubbard band in the TD-PES spectra, and showed that this is a direct effect of the Hund's coupling. The experimental observation of such a dynamic splitting would be a "smoking gun" experiment for nonequilibrium Hund's physics. Note that, although these features have two orders of magnitude lower intensity than the filled lower Hubbard band in the TD-PES spectra (Fig. 4), the photo doping density in the upper Hubbard band can be detected experimentally, see, e.g., recent work on tantalum disulfide ($1T$-TaS_2) [5].

By studying the time evolution of the local many-body states, we also identified two distinct multiorbital Hund's coupling effects, which we denoted *thermal blocking* and *kinetic freezing*. Thermal blocking in the photodoping dynamics arises when the temperature of the initial state competes with the Hund's splitting of the local states, $T \gtrsim J$, inhibiting the dynamics of thermally occupied local spin excitations. The kinetic freezing effect on the other hand is the competition between the Hund's coupling J and the bandwidth W of the electronic hopping. In the regime $W \lesssim J$, the internal dynamics of the local spin excitations are frozen out since the available kinetic energy is less than the energy J or $3J$ required to generate such spin excitations.

An interesting venue for further studies is the photodoping of the anti-ferromagnetic state, and its characteristic changes with temperature. In this case, there is an additional energy scale (the antiferromagnetic exchange coupling J_{ex}), and the relaxation dynamics will depend on the relative values of T, W, J, and J_{ex}. It should also be interesting to investigate the quantitative changes in the dynamics of the two-band model when going from the density-density interaction case studied here to the rotationally invariant Kanamori interaction (setting $\gamma = 1$ in Eq. [2]). Since this changes the degeneracy of the doublon states and modifies the multiplet splittings [62], from J and $3J$ to $2J$ and $4J$, we expect the onset of *thermal blocking* and *kinetic freezing* to shift.

An interesting material to explore some of the Hund's coupling effects discussed in this paper is the paramagnetic Mott insulator Ca_2RuO_4. A recent ARPES study of this material, and a combined density functional theory plus DMFT investigation [77] suggest that spectral features originating from the Hund's coupling are present already in equilibrium. Since the proposed effective local interaction parameters for this system yield $J/U \approx 0.17$ we predict that a time-dependent photo emission study with pump excitation across the Mott gap of ≈2.7 eV should produce a pronounced splitting in the photocarrier distribution in the upper Hubbard band, qualitatively similar to what we observe in Figs. 4(c) and 4(d).

ACKNOWLEDGMENTS

The calculations have been performed on the UniFr cluster. H.U.R.S., D.G., and P.W. were supported by the European Research Council under the European Union's Seventh Framework Programme (FP7/2007-2013) / ERC Starting Grant No. 278023 and the Swiss National Science Foundation (Grant No. 200021-140648). H.U.R.S. was also supported by the Swiss National Science Foundation through NCCR MARVEL.

APPENDIX A: LOCAL MANY-BODY VIEW ON RELAXATION

The pseudoparticle approach does not only give access to the local many-body density matrix, but also to spectroscopic information on the local many-body states (the pseudoparticles). The equilibrium pseudoparticle spectral functions $\hat{G}_\Gamma(\omega,t)$ for all local many-body states Γ are shown in Fig. 11(a). The three doublon states, the high-spin $S = 1$ state (green), and the high- (yellow) and low-energy (red) $S = 0$ doublon states (split by J and $3J$) are the lowest-energy

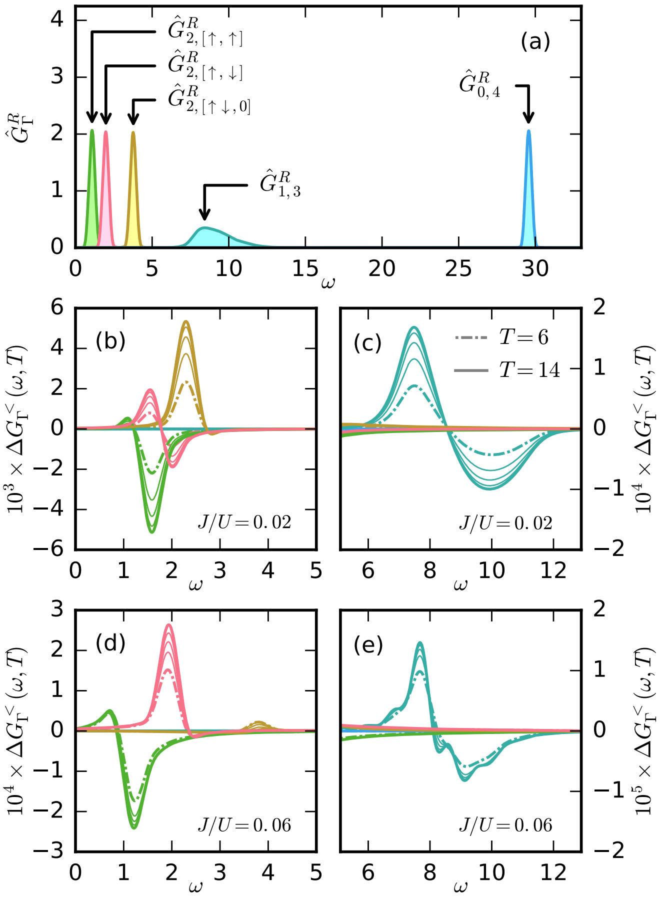

FIG. 11. Equilibrium pseudoparticle frequency Green's function $\hat{G}^R_\Gamma(\omega)$ for $U=15$, $\beta=1$, $J/U=0.06$ (a). [(b)–(e)] Change in the lesser pseudoparticle Green's function, $\Delta G^<_\Gamma(\omega,T) = G^<_\Gamma(\omega,T) - G^<_\Gamma(\omega,4)$, relative to absolute time $T=4$ for times $T=6,8,10,12,14$, for $J/U=0.02$ [(b) and (c)] and $J/U=0.06$ [(d) and (e)].

pseudoparticles at half-filling. The singlon-triplon states are intermediate in energy (at $\omega \approx 10$) and the holon-quadruplon states (at $\omega \approx 30$) are the highest energy local many-body states. The singlon-triplon states are the only ones that are dispersive, with a smeared-out spectral distribution. All other states, the doublons and holon-quadruplons are delta-peak-like resonances (the peak widths in Fig. 11 are due to a limited frequency resolution).

Since only the singlon-triplon states are dispersive, kinetic energy relaxation is restricted to these states. Hence the singlon-triplon scattering processes (IIa and IIb), schematically shown in Fig. 1, are the relevant processes for relaxing excess kinetic energy in the photodoped Mott insulator. This can also be seen in the time-dependent change in the singlon-triplon occupied density of states [Fig. 11(c)], where spectral density is redistributed with time from high to low frequencies within the singlon-triplon pseudoparticle band. As previously noted, the speed of the kinetic relaxation is controlled by the Hund's coupling J and comparing $J/U = 0.02$ and 0.06 the relaxation is only visible in the time range $t = 6$ to 14 for the lower value of J, compare Figs. 11(c) and 11(e) [note the order-of-magnitude scale difference between panels (b), (d) and (c), (e)].

The redistribution within the doublon sector can also be analyzed in terms of the time-dependent pseudoparticle spectral function, see Figs. 11(b) and 11(d). For $J/U = 0.02$ [Fig. 11(b)], we observe the redistribution from the high-spin $S=1$ doublon (green) to the high-energy $S=0$ doublon (yellow), while the spectral weight of the low-energy $S=0$ doublon (red) shifts down in energy. For $J/U=0.06$ [Fig. 11(d)] the situation is markedly different. The high-energy $S=0$ doublon (yellow) is now well separated from the $S=1$ and low-energy $S=0$ doublons (green and red) and only a conversion between the last two occurs on the time scale of the calculations. This is a prime example of *kinetic freezing* of the high-energy doublon state.

We also note that the pseudoparticle spectral function enables a qualitative understanding of the single-particle spectral function. In particular, the three-peak structure in the upper Hubbard band of Fig. 5(g), corresponding to the removal processes $|3\rangle \to |2,\Gamma\rangle$, can be understood as the convolution of the lesser triplon spectral function $\hat{G}^<_{0,3}$ and the retarded doublon spectral functions $\hat{G}^R_{2,\Gamma}$.

APPENDIX B: PSEUDOPARTICLE STRONG-COUPLING-DIAGRAM SYMMETRY ANALYSIS

While it is straightforward to write down all symmetry allowed pseudoparticle strong coupling self-energy and single-particle Green's function diagrams in, e.g, the DMFT approach for the single-band Hubbard model, the number of possible diagrams and symmetries proliferate when going to multiorbital systems, general interactions, and spontaneous symmetry broken states. In order to exploit (simple) symmetries in the diagrams and thereby reduce the computational effort, we have implemented an automated numerical symmetry analysis for the first- and second-order diagrams.

The approach builds on top of the standard block diagonalization of the local Hamiltonian, $H_{\Gamma\Gamma'} \to H_{s,\Gamma\Gamma'}$, and the pseudoparticle propagator $\hat{G}(t_1,t_2) \equiv \hat{G}(12) \to \hat{G}_{s,\Gamma\Gamma'}(12)$ into blocks s of Hilbert space states Γ [48]. This procedure is analogous to the block diagonalization employed in the continuous-time quantum Monte Carlo hybridization expansion, see Section X.F.1 in Ref. [64] for an in-depth discussion. The blocks are constructed so that each block s is only connected to a single other block s' by the application of a creation or annihilation operator $c_a \equiv c_{\alpha\sigma}$ and $c^\dagger_{\bar{a}} = c^\dagger_{\alpha\sigma}$, where a is a super index containing orbital (α) and spin (σ) indices.

Using the matrix notation developed in Ref. [78] the pseudoparticle strong coupling first-order self-energy $\hat{\Sigma}^{\mathrm{NCA}}$ (i.e., the noncrossing approximation, NCA) takes the form

$$\hat{\Sigma}^{\mathrm{NCA}}(12) = i \sum_{\bar{a}b} (\Delta_{\bar{a}b}(12)[c^\dagger_{\bar{a}} \hat{G}(12) c_b] - \Delta_{\bar{a}b}(21)[c_b \hat{G}(12) c^\dagger_{\bar{a}}]), \tag{B1}$$

see Appendix B in Ref. [78]. Using the blocking of the local Hilbert space the self-energy $\hat{\Sigma}^{\mathrm{NCA}}_s(12)$ of the block s can be written as

$$\hat{\Sigma}^{\mathrm{NCA}}_s(12) = \sum_{\bar{a}b} \sum_{\bar{s}} \sum_{\eta=\leftarrow,\rightarrow} \hat{\mathcal{S}}^{\mathrm{NCA}}_{s\bar{s},\eta,\bar{a}b}(12), \tag{B2}$$

```
Data: All diagram indices $\gamma = \{s\bar{s}, \eta, \bar{a}b\}$
Result: The set $\mathcal{U}$ and the factors $C_{s,\gamma'}$
$\mathcal{U} = []$;
for all $\gamma = \{s\bar{s}, \eta, \bar{a}b\}$ do
    calculate $\hat{\mathcal{S}}_\gamma$;
    for $\gamma' \in \mathcal{U}$ do
        if $\hat{\mathcal{S}}_\gamma = \hat{\mathcal{S}}_{\gamma'}$ then
            $C_{s_\gamma,\gamma'}$ += 1;
        else if $\hat{\mathcal{S}}_\gamma = -\hat{\mathcal{S}}_{\gamma'}$ then
            $C_{s_\gamma,\gamma'}$ −= 1;
        else
            append $\gamma$ to $\mathcal{U}$;
            for $s$ in all Hilbert space blocks do
                $C_{s,\gamma} = 0$;
            end
            $C_{s_\gamma,\gamma} = 1$;
        end
    end
end
```

FIG. 12. Algorithm for the PPSC first-order (NCA) self-energy diagram symmetry analysis.

where $\hat{\mathcal{S}}^{\mathrm{NCA}}_{s\bar{s},\eta,\bar{a}b}(12)$ are the single self-energy diagram contributions

$$\hat{\mathcal{S}}^{\mathrm{NCA}}_{s\bar{s},\leftarrow,\bar{a}b}(12) \equiv +i\,\Delta_{\bar{a}b}(12)[(c^\dagger_{\bar{a}})_{s\bar{s}}\,\hat{G}_{\bar{s}}(12)\,(c_b)_{\bar{s}s}], \tag{B3}$$

$$\hat{\mathcal{S}}^{\mathrm{NCA}}_{s\bar{s},\rightarrow,\bar{a}b}(12) \equiv -i\,\Delta_{\bar{a}b}(21)[(c_b)_{s\bar{s}}\,\hat{G}_{\bar{s}}(12)\,(c^\dagger_{\bar{a}})_{\bar{s}s}], \tag{B4}$$

with a forward ($\eta = \leftarrow$) or backward ($\eta = \rightarrow$) propagating insertion of the hybridization function $\Delta_{\bar{a}b}$.

The automatic symmetry analysis involves two steps. First, it performs a short-time propagation of all the diagram contributions $\hat{\mathcal{S}}^{\mathrm{NCA}}_{s\bar{s},\eta,\bar{a}b}(12)$. Then, the contributions are compared and classified to be equal or different (up to a sign and a fixed numerical accuracy). We then construct a set $\mathcal{U}^{\mathrm{NCA}}_\Sigma$ of indices $\gamma = \{\eta,\bar{a}b,s\bar{s}\} \in \mathcal{U}^{\mathrm{NCA}}_\Sigma$ with only one diagram representative from each class, and for each such index γ we store the class' contribution to each self-energy sector s' in the scalar factors $C^{\mathrm{NCA}}_{s',\gamma}$. These steps are detailed in Fig. 12.

For the long-time simulations, this information is used to calculate one and only one unique diagram $\hat{\mathcal{S}}^{\mathrm{NCA}}_\gamma$ per diagram class, which allows to calculate the self-energy as the symmetry reduced sum

$$\hat{\Sigma}^{\mathrm{NCA}}_s(12) = \sum_{\gamma \in \mathcal{U}^{\mathrm{NCA}}_\Sigma} C^{\mathrm{NCA}}_{s,\gamma}\hat{\mathcal{S}}^{\mathrm{NCA}}_\gamma(12). \tag{B5}$$

This approach substantially speeds up the calculations in symmetric cases such as particle-hole symmetry, spin degeneracy, etc., while also allowing the study of situations with no or reduced symmetry.

1. Second-order pseudoparticle self energy

The symmetry analysis is general and also applicable to the second-order PPSC self-energy $\hat{\Sigma}^{\mathrm{OCA}}(12)$ (i.e., the one-crossing approximation, OCA). At second order, the diagrams contain two crossing hybridization-function insertions, which yields four directed diagram contributions

$$\begin{aligned}
&\hat{\Sigma}^{\mathrm{OCA}}(14)\\
&\quad = \sum_{\bar{a}b}\sum_{\bar{c}d}\int d2d3\,(+\Delta_{\bar{a}b}(13)\Delta_{\bar{c}d}(24)\\
&\qquad \times [c^\dagger_{\bar{a}}\hat{G}(12)c^\dagger_{\bar{c}}\hat{G}(23)c_b\hat{G}(34)c_d]\\
&\qquad - \Delta_{\bar{a}b}(13)\Delta_{\bar{c}d}(42)[c^\dagger_{\bar{a}}\hat{G}(12)c_d\hat{G}(23)c_b\hat{G}(34)c^\dagger_{\bar{c}}]\\
&\qquad - \Delta_{\bar{a}b}(31)\Delta_{\bar{c}d}(24)[c_b\hat{G}(12)c^\dagger_{\bar{c}}\hat{G}(23)c^\dagger_{\bar{a}}\hat{G}(34)c_d]\\
&\qquad + \Delta_{\bar{a}b}(31)\Delta_{\bar{c}d}(42)[c_b\hat{G}(12)c_d\hat{G}(23)c^\dagger_{\bar{a}}\hat{G}(34)c^\dagger_{\bar{c}}]).
\end{aligned} \tag{B6}$$

When introducing the Hilbert space blocks s, the complete sum takes the form

$$\hat{\Sigma}^{\mathrm{OCA}}_s(14) = \sum_{\bar{a}b\bar{c}d}\sum_{s_1s_2s_3}\sum_{\eta}\int d2d3\,\hat{\mathcal{S}}^{\mathrm{OCA}}_{s,s_1s_2s_3,\eta,\bar{a}b\bar{c}d}(1234), \tag{B7}$$

with the four directional contributions

$$\hat{\mathcal{S}}^{\mathrm{OCA}}_{s,s_1s_2s_3,\leftarrow\leftarrow,\bar{a}b\bar{c}d}(1234) \equiv +\Delta_{\bar{a}b}(13)\Delta_{\bar{c}d}(24)\big[(c^\dagger_{\bar{a}})_{ss_1}\hat{G}_{s_1}(12)(c^\dagger_{\bar{c}})_{s_1s_2}\hat{G}_{s_2}(23)(c_b)_{s_2s_3}\hat{G}_{s_3}(34)(c_d)_{s_3s}\big], \tag{B8}$$

$$\hat{\mathcal{S}}^{\mathrm{OCA}}_{s,s_1s_2s_3,\leftarrow\rightarrow,\bar{a}b\bar{c}d}(1234) \equiv -\Delta_{\bar{a}b}(13)\Delta_{\bar{c}d}(42)\big[(c^\dagger_{\bar{a}})_{ss_1}\hat{G}_{s_1}(12)(c_d)_{s_1s_2}\hat{G}_{s_2}(23)(c_b)_{s_2s_3}\hat{G}_{s_3}(34)(c^\dagger_{\bar{c}})_{s_3s}\big], \tag{B9}$$

$$\hat{\mathcal{S}}^{\mathrm{OCA}}_{s,s_1s_2s_3,\rightarrow\leftarrow,\bar{a}b\bar{c}d}(1234) \equiv -\Delta_{\bar{a}b}(31)\Delta_{\bar{c}d}(24)\big[(c_b)_{ss_1}\hat{G}_{s_1}(12)(c^\dagger_{\bar{c}})_{s_1s_2}\hat{G}_{s_2}(23)(c^\dagger_{\bar{a}})_{s_2s_3}\hat{G}_{s_3}(34)(c_d)_{s_3s}\big], \tag{B10}$$

$$\hat{\mathcal{S}}^{\mathrm{OCA}}_{s,s_1s_2s_3,\rightarrow\rightarrow,\bar{a}b\bar{c}d}(1234) \equiv +\Delta_{\bar{a}b}(31)\Delta_{\bar{c}d}(42)\big[(c_b)_{ss_1}\hat{G}_{s_1}(12)(c_d)_{s_1s_2}\hat{G}_{s_2}(23)(c^\dagger_{\bar{a}})_{s_2s_3}\hat{G}_{s_3}(34)(c^\dagger_{\bar{c}})_{s_3s}\big]. \tag{B11}$$

Also, in this case, all diagram contributions $\hat{\mathcal{S}}^{\mathrm{OCA}}_\nu(12) \equiv \int d2d3\,\hat{\mathcal{S}}^{\mathrm{OCA}}_{s,s_1s_2s_3,\eta,\bar{a}b\bar{c}d}(1234)$ are calculated for a short-time evolution and separated in classes represented by a unique index combination $\nu = \{\eta,\bar{a}b\bar{c}d,s,s_1s_2s_3\}$ and scalar weight factors $C^{\mathrm{OCA}}_{s,\nu}$ giving $\hat{\Sigma}^{\mathrm{OCA}}_s$ as a sum analogous to Eq. (B5),

$$\hat{\Sigma}^{\mathrm{OCA}}_s(12) = \sum_{\nu \in \mathcal{U}^{\mathrm{OCA}}_\Sigma} C^{\mathrm{OCA}}_{s,\nu}\hat{\mathcal{S}}^{\mathrm{OCA}}_\nu(12). \tag{B12}$$

2. Single-particle Green's function

The first- and second-order diagrams for the single-particle Green's function $g_{a\bar{b}}(12)$ can analogously be decomposed into diagram contributions:

$$\mathcal{G}^{\mathrm{NCA}}_\gamma(12) \equiv \mathcal{G}^{\mathrm{NCA}}_{s_1s_2,a\bar{b}}(12) \tag{B13}$$

$$\mathcal{G}^{\mathrm{OCA}}_\nu(12) \equiv \int d\bar{1}d\bar{2}\,\mathcal{G}^{\mathrm{OCA}}_{s_1s_2s_3s_4,\eta,a\bar{b}c\bar{d}}(1\bar{1}\bar{2}2), \tag{B14}$$

respectively. The first-order (NCA) contribution to $g_{a\bar{b}}(12)$ is given by the expression

$$g^{\mathrm{NCA}}_{a\bar{b}}(12) = \mathrm{Tr}[i\hat{G}(21)c_a\hat{G}(12)c^\dagger_{\bar{b}}] = \sum_{s_1 s_2} \mathcal{G}^{\mathrm{NCA}}_{s_1 s_2, a\bar{b}}(12), \tag{B15}$$

see Appendix B in Ref. [78], where the diagram contributions $\mathcal{G}^{\mathrm{NCA}}_{s_1 s_2, a\bar{b}}(12)$ are given by

$$\mathcal{G}^{\mathrm{NCA}}_{s_1 s_2, a\bar{b}}(12) \equiv \mathrm{Tr}\big[i\hat{G}_{s_1}(21)\,(c_a)_{s_1 s_2}\,\hat{G}_{s_2}(12)\,(c^\dagger_{\bar{b}})_{s_2 s_1}\big]. \tag{B16}$$

The second-order (OCA) contribution on the other hand contains a directed internal hybridization insertion, yielding the closed bubble diagrams

$$g^{\mathrm{OCA}}_{a\bar{b}}(13) = \sum_{\bar{c}d} \int d2d4\,(-\Delta_{\bar{c}d}(24)\mathrm{Tr}[\hat{G}(41)c_a\hat{G}(12)c^\dagger_{\bar{c}}\hat{G}(23)c^\dagger_{\bar{b}}\hat{G}(34)c_d] - \Delta_{\bar{c}d}(42)\mathrm{Tr}[\hat{G}(41)c_a\hat{G}(12)c_d\hat{G}(23)c^\dagger_{\bar{b}}\hat{G}(34)c^\dagger_{\bar{c}}]), \tag{B17}$$

whose contributions can be collected as

$$g^{\mathrm{OCA}}_{a\bar{b}}(13) = \sum_{\bar{c}d} \sum_{s_1 s_2 s_3 s_4} \sum_{\eta} \int d2d4\,\mathcal{G}^{\mathrm{OCA}}_{s_1 s_2 s_3 s_4, \eta, a\bar{b}\bar{c}d}(1234), \tag{B18}$$

where the forward ($\eta = \leftarrow$) and backward ($\eta = \rightarrow$) contributions are defined as

$$\mathcal{G}^{\mathrm{OCA}}_{s_1 s_2 s_3 s_4, \leftarrow, a\bar{b}\bar{c}d}(1234) \equiv -\Delta_{\bar{c}d}(24)\mathrm{Tr}\big[\hat{G}_{s_1}(41)(c_a)_{s_1 s_2}\hat{G}_{s_2}(12)(c^\dagger_{\bar{c}})_{s_2 s_3}\hat{G}_{s_3}(23)(c^\dagger_{\bar{b}})_{s_3 s_4}\hat{G}_{s_4}(34)(c_d)_{s_4 s_1}\big], \tag{B19}$$

$$\mathcal{G}^{\mathrm{OCA}}_{s_1 s_2 s_3 s_4, \rightarrow, a\bar{b}\bar{c}d}(1234) \equiv -\Delta_{\bar{c}d}(42)\mathrm{Tr}\big[\hat{G}_{s_1}(41)(c_a)_{s_1 s_2}\hat{G}_{s_2}(12)(c_d)_{s_2 s_3}\hat{G}_{s_3}(23)(c^\dagger_{\bar{b}})_{s_3 s_4}\hat{G}_{s_4}(34)(c^\dagger_{\bar{c}})_{s_4 s_1}\big]. \tag{B20}$$

The symmetry reduction proceeds in exactly the same way as for the self-energy diagrams by mapping each unique diagram class' contribution $\mathcal{G}^{\mathrm{NCA}}_{\gamma}(12)$ and $\mathcal{G}^{\mathrm{OCA}}_{\nu}(12)$ (with $\gamma = \{a\bar{b}, s_1 s_2\}$ and $\nu = \{\eta, a\bar{b}\bar{c}d, s_1 s_2 s_3 s_4\}$) to $g_{a\bar{b}}(12)$ through scalar factors, $C^{\mathrm{NCA}}_{a\bar{b},\gamma}$ and $C^{\mathrm{OCA}}_{a\bar{b},\nu}$ respectively, i.e.,

$$g_{a\bar{b}}(12) = \sum_{\gamma \in \mathcal{U}^{\mathrm{NCA}}_g} C^{\mathrm{NCA}}_{a\bar{b},\gamma}\mathcal{G}^{\mathrm{NCA}}_{\gamma}(12) + \sum_{\nu \in \mathcal{U}^{\mathrm{OCA}}_g} C^{\mathrm{OCA}}_{a\bar{b},\nu}\mathcal{G}^{\mathrm{OCA}}_{\nu}(12). \tag{B21}$$

Also for the single-particle Green's function $g_{a\bar{b}}(12)$, the number of components γ and ν that needs to be evaluated is reduced for systems with symmetries, such as, particle-hole symmetry (when the forward and backwards contributions are equal), and orbital degeneracy where all spin-orbital index pairs $a\bar{a}$ are equal.

[1] S. Iwai, M. Ono, A. Maeda, H. Matsuzaki, H. Kishida, H. Okamoto, and Y. Tokura, Phys. Rev. Lett. **91**, 057401 (2003).

[2] H. Okamoto, T. Miyagoe, K. Kobayashi, H. Uemura, H. Nishioka, H. Matsuzaki, A. Sawa, and Y. Tokura, Phys. Rev. B **82**, 060513 (2010).

[3] L. Perfetti, P. A. Loukakos, M. Lisowski, U. Bovensiepen, H. Berger, S. Biermann, P. S. Cornaglia, A. Georges, and M. Wolf, Phys. Rev. Lett. **97**, 067402 (2006).

[4] L. Perfetti, P. A. Loukakos, M. Lisowski, U. Bovensiepen, M. Wolf, H. Berger, S. Biermann, and A. Georges, New J. Phys. **10**, 053019 (2008).

[5] M. Ligges, I. Avigo, D. Golež, H. Strand, L. Stojchevska, M. Kalläne, K. Rossnagel, M. Eckstein, P. Werner, and U. Bovensiepen, arXiv:1702.05300 [cond-mat.str-el].

[6] S. L. Johnson, R. A. de Souza, U. Staub, P. Beaud, E. Möhr-Vorobeva, G. Ingold, A. Caviezel, V. Scagnoli, W. F. Schlotter, J. J. Turner, O. Krupin, W.-S. Lee, Y.-D. Chuang, L. Patthey, R. G. Moore, D. Lu, M. Yi, P. S. Kirchmann, M. Trigo, P. Denes, D. Doering, Z. Hussain, Z.-X. Shen, D. Prabhakaran, and A. T. Boothroyd, Phys. Rev. Lett. **108**, 037203 (2012).

[7] J. A. Johnson, T. Kubacka, M. C. Hoffmann, C. Vicario, S. de Jong, P. Beaud, S. Grübel, S.-W. Huang, L. Huber, Y. W. Windsor, E. M. Bothschafter, L. Rettig, M. Ramakrishnan, A. Alberca, L. Patthey, Y.-D. Chuang, J. J. Turner, G. L. Dakovski, W.-S. Lee, M. P. Minitti, W. Schlotter, R. G. Moore, C. P. Hauri, S. M. Koohpayeh, V. Scagnoli, G. Ingold, S. L. Johnson, and U. Staub, Phys. Rev. B **92**, 184429 (2015).

[8] P. B. Allen, Phys. Rev. Lett. **59**, 1460 (1987).

[9] S. D. Brorson, A. Kazeroonian, J. S. Moodera, D. W. Face, T. K. Cheng, E. P. Ippen, M. S. Dresselhaus, and G. Dresselhaus, Phys. Rev. Lett. **64**, 2172 (1990).

[10] C. Gadermaier, A. S. Alexandrov, V. V. Kabanov, P. Kusar, T. Mertelj, X. Yao, C. Manzoni, D. Brida, G. Cerullo, and D. Mihailovic, Phys. Rev. Lett. **105**, 257001 (2010).

[11] E. van Heumen, E. Muhlethaler, A. B. Kuzmenko, H. Eisaki, W. Meevasana, M. Greven, and D. van der Marel, Phys. Rev. B **79**, 184512 (2009).

[12] J. D. Rameau, S. Freutel, A. F. Kemper, M. A. Sentef, J. K. Freericks, I. Avigo, M. Ligges, L. Rettig, Y. Yoshida, H. Eisaki, J. Schneeloch, R. D. Zhong, Z. J. Xu, G. D. Gu, P. D. Johnson, and U. Bovensiepen, Nat. Commun. **7**, 13761 EP (2016).

[13] S. Dal Conte, C. Giannetti, G. Coslovich, F. Cilento, D. Bossini, T. Abebaw, F. Banfi, G. Ferrini, H. Eisaki, M. Greven, A. Damascelli, D. van der Marel, and F. Parmigiani, Science **335**, 1600 (2012).

[14] S. Dal Conte, L. Vidmar, D. Golez, M. Mierzejewski, G. Soavi, S. Peli, F. Banfi, G. Ferrini, R. Comin, B. M. Ludbrook, L. Chauviere, N. D. Zhigadlo, H. Eisaki, M. Greven, S. Lupi, A. Damascelli, D. Brida, M. Capone, J. Bonca, G. Cerullo, and C. Giannetti, Nat. Phys. **11**, 421 (2015).

[15] M. Porer, U. Leierseder, J. M. Ménard, H. Dachraoui, L. Mouchliadis, I. E. Perakis, U. Heinzmann, J. Demsar, K. Rossnagel, and R. Huber, Nat. Mater. **13**, 857 (2014).

[16] E. Fradkin, S. A. Kivelson, and J. M. Tranquada, Rev. Mod. Phys. **87**, 457 (2015).

[17] H. Aoki, N. Tsuji, M. Eckstein, M. Kollar, T. Oka, and P. Werner, Rev. Mod. Phys. **86**, 779 (2014).

[18] A. F. Kemper, M. A. Sentef, B. Moritz, T. P. Devereaux, and J. K. Freericks, arXiv:1609.00087 [cond-mat.supr-con].

[19] N. Strohmaier, D. Greif, R. Jördens, L. Tarruell, H. Moritz, T. Esslinger, R. Sensarma, D. Pekker, E. Altman, and E. Demler, Phys. Rev. Lett. **104**, 080401 (2010).

[20] M. Eckstein and P. Werner, Phys. Rev. B **84**, 035122 (2011).

[21] Z. Lenarčič and P. Prelovšek, Phys. Rev. Lett. **111**, 016401 (2013).

[22] P. Werner, K. Held, and M. Eckstein, Phys. Rev. B **90**, 235102 (2014).

[23] M. Eckstein and P. Werner, Phys. Rev. Lett. **110**, 126401 (2013).

[24] P. Werner, N. Tsuji, and M. Eckstein, Phys. Rev. B **86**, 205101 (2012).

[25] D. Golež, M. Eckstein, and P. Werner, Phys. Rev. B **92**, 195123 (2015).

[26] P. Werner and M. Eckstein, Europhys. Lett. **109**, 37002 (2015).

[27] F. Dorfner, L. Vidmar, C. Brockt, E. Jeckelmann, and F. Heidrich-Meisner, Phys. Rev. B **91**, 104302 (2015).

[28] S. Sayyad and M. Eckstein, Phys. Rev. B **91**, 104301 (2015).

[29] Y. Murakami, P. Werner, N. Tsuji, and H. Aoki, Phys. Rev. B **91**, 045128 (2015).

[30] D. Golež, J. Bonča, L. Vidmar, and S. A. Trugman, Phys. Rev. Lett. **109**, 236402 (2012).

[31] M. Eckstein and P. Werner, Sci. Rep. **6**, 21235 EP (2016).

[32] D. Golež, J. Bonča, M. Mierzejewski, and L. Vidmar, Phys. Rev. B **89**, 165118 (2014).

[33] D. Golez, L. Boehnke, H. Strand, M. Eckstein, and P. Werner, Phys. Rev. Lett. **118**, 246402 (2017).

[34] P. Werner and M. Eckstein, Struct. Dyn. **3**, 023603 (2016).

[35] S. Sugano, Y. Tanabe, and H. Kamimura, *Multiplets of Transition-Metal Ions in Crystals* (Academic Press Inc., New York, 1970).

[36] J. Kanamori, Prog. Theor. Phys. **30**, 275 (1963).

[37] S. Hoshino and P. Werner, Phys. Rev. B **93**, 155161 (2016).

[38] K. Steiner, S. Hoshino, Y. Nomura, and P. Werner, Phys. Rev. B **94**, 075107 (2016).

[39] N. Tsuji and P. Werner, Phys. Rev. B **88**, 165115 (2013).

[40] N. Tsuji, M. Eckstein, and P. Werner, Phys. Rev. Lett. **110**, 136404 (2013).

[41] E. v. Oelsen, G. Seibold, and J. Bünemann, Phys. Rev. Lett. **107**, 076402 (2011).

[42] E. von Oelsen, G. Seibold, and J. Bünemann, New J. Phys. **13**, 113031 (2011).

[43] M. Behrmann, M. Fabrizio, and F. Lechermann, Phys. Rev. B **88**, 035116 (2013).

[44] M. Behrmann and F. Lechermann, Phys. Rev. B **91**, 075110 (2015).

[45] M. Sandri and M. Fabrizio, Phys. Rev. B **91**, 115102 (2015).

[46] M. Behrmann, A. I. Lichtenstein, M. I. Katsnelson, and F. Lechermann, Phys. Rev. B **94**, 165120 (2016).

[47] G. Mazza and A. Georges, Phys. Rev. B **96**, 064515 (2017).

[48] M. Eckstein and P. Werner, Phys. Rev. B **82**, 115115 (2010).

[49] G. Baym and L. P. Kadanoff, Phys. Rev. **124**, 287 (1961).

[50] G. Baym, Phys. Rev. **127**, 1391 (1962).

[51] H. Brunner and P. J. van der Houwen, *The Numerical Solution of Volterra Equations* (North-Holland, Amsterdam, 1986).

[52] We use an implicit fifth-order multistep method to solve the integrodifferential Dyson equation [17] on an equidistant grid in both imaginary and real time employing backward differentiation for the derivative and Gregory weights for the integrals, for the relevant nomenclature see Ref. [51]. The warmup steps and the imaginary time integrals are performed using a hybrid integration scheme employing Gregory weights and direct polynomial interpolation on intervals containing less points than the approximation order.

[53] The memory footprint of two-time Green's functions scales quadratically $\mathcal{O}(N_t^2)$ with the number of time steps N_t, while the scaling with the number of single-particle orbitals N_{orb} in PPSC is, in the case considered here with density-density interaction, linear in the size of the related local many-body Fock space $N_\Gamma \equiv 2^{2N_{\text{orb}}}$, giving an overall scaling $\mathcal{O}(N_t^2 N_\Gamma) \equiv \mathcal{O}(N_t^2 \cdot 2^{2N_{\text{orb}}})$.

[54] A. Koga, K. Inaba, and N. Kawakami, Prog. Theor. Phys. **160**, 253 (2005).

[55] T. Pruschke and R. Bulla, Eur. Phys. J. B **44**, 217 (2005).

[56] P. Werner and A. J. Millis, Phys. Rev. B **74**, 155107 (2006).

[57] S. Sakai, R. Arita, K. Held, and H. Aoki, Phys. Rev. B **74**, 155102 (2006).

[58] P. Werner and A. J. Millis, Phys. Rev. Lett. **99**, 126405 (2007).

[59] R. Bulla, T. A. Costi, and T. Pruschke, Rev. Mod. Phys. **80**, 395 (2008).

[60] R. Peters and T. Pruschke, Phys. Rev. B **81**, 035112 (2010).

[61] R. Peters, N. Kawakami, and T. Pruschke, Phys. Rev. B **83**, 125110 (2011).

[62] A. E. Antipov, I. S. Krivenko, V. I. Anisimov, A. I. Lichtenstein, and A. N. Rubtsov, Phys. Rev. B **86**, 155107 (2012).

[63] P. Werner, A. Comanac, L. de' Medici, M. Troyer, and A. J. Millis, Phys. Rev. Lett. **97**, 076405 (2006).

[64] E. Gull, A. J. Millis, A. I. Lichtenstein, A. N. Rubtsov, M. Troyer, and P. Werner, Rev. Mod. Phys. **83**, 349 (2011).

[65] P. Seth, I. Krivenko, M. Ferrero, and O. Parcollet, Comp. Phys. Commun. **200**, 274 (2016).

[66] O. Parcollet, M. Ferrero, T. Ayral, H. Hafermann, I. Krivenko, L. Messio, and P. Seth, Comput. Phys. Commun. **196**, 398 (2015).

[67] L. Boehnke, H. Hafermann, M. Ferrero, F. Lechermann, and O. Parcollet, Phys. Rev. B **84**, 075145 (2011).

[68] H. U. R. Strand, M. Eckstein, and P. Werner, Phys. Rev. A **92**, 063602 (2015).

[69] G. Auböck, C. Consani, F. van Mourik, and M. Chergui, Opt. Lett. **37**, 2337 (2012).

[70] E. Baldini, L. Chiodo, A. Dominguez, M. Palummo, S. Moser, M. Yazdi-Rizi, G. Auböck, B. P. P. Mallett, H. Berger, A. Magrez, C. Bernhard, M. Grioni, A. Rubio, and M. Chergui, Nat. Commun. **8**, 13 (2017).

[71] E. Baldini, A. Mann, L. Benfatto, E. Cappelluti, A. Acocella, V. M. Silkin, S. V. Eremeev, A. B. Kuzmenko, S. Borroni, T. Tan, X. X. Xi, F. Zerbetto, R. Merlin, and F. Carbone, Phys. Rev. Lett. **119**, 097002 (2017).

[72] R. Sensarma, D. Pekker, E. Altman, E. Demler, N. Strohmaier, D. Greif, R. Jördens, L. Tarruell, H. Moritz, and T. Esslinger, Phys. Rev. B **82**, 224302 (2010).

[73] Z. Lenarčič and P. Prelovšek, Phys. Rev. B **90**, 235136 (2014).

[74] J. K. Freericks, H. R. Krishnamurthy, and T. Pruschke, Phys. Rev. Lett. **102**, 136401 (2009).

[75] P. Werner and M. Eckstein, Phys. Rev. B **88**, 165108 (2013).

[76] H. U. R. Strand, Phys. Rev. B **90**, 155108 (2014).

[77] D. Sutter, C. G. Fatuzzo, S. Moser, M. Kim, R. Fittipaldi, A. Vecchione, V. Granata, Y. Sassa, F. Cossalter, G. Gatti, M. Grioni, H. M. Ronnow, N. C. Plumb, C. E. Matt, M. Shi, M. Hoesch, T. K. Kim, T. R. Chang, H. T. Jeng, C. Jozwiak, A. Bostwick, E. Rotenberg, A. Georges, T. Neupert, and J. Chang, Nat. Commun. **8**, 15176 (2017).

[78] H. U. R. Strand, M. Eckstein, and P. Werner, Phys. Rev. X **5**, 011038 (2015).